Structure and collective excitations of ^{4}He clusters

S. A. Chin
Center for Theoretical Physics and Department of Physics, Texas A&M University, College Station, Texas 77843

E. Krotscheck
Center for Theoretical Physics and Department of Physics, Texas A&M University, College Station, Texas 77843 and Theoretical Physics Institute and Minnesota Supercomputer Institute, University of Minnesota, Minneapolis, Minnesota 55455

(Received 19 August 1991)

We compute zero-temperature ground-state energies, one- and two-body densities, collective-excitation spectra, transition densities, and static and dynamic structure functions of ^{4}He clusters up to a cluster size of $N=112$ particles. The ground-state properties are computed using a second-order diffusion Monte Carlo algorithm with Jastrow and triplet trial functions used for importance sampling. Excitation energies, transition densities, and dynamic structure functions are obtained by solving a generalized Feynman eigenvalue equation. We determine the systematic variation of collective energies with cluster size, demonstrate the existence of persistent oscillations in transition densities, evaluate the strength of collective modes quantitatively, and show how the cluster continuum excitation spectrum can be directly mapped by the dynamic structure function. By comparison with the full static structure function, the collective quadrupole state is found to exhaust approximately 25% of the total strength.

I. INTRODUCTION

The study of finite ^{4}He clusters and, more generally, quantum liquids in confined geometries, is currently an active area of experimental[1,2] and theoretical[3–11] research. Helium clusters are unique in that they are the only known *bosonic*, but fully quantum, finite systems. Because of the simplicity of the ^{4}He-^{4}He potential, helium clusters are excellent laboratories for the study of finite quantum many-particle systems. In this case, unlike that of nuclei, it is possible to calculate intrinsic many-body effects microscopically, unhampered by the complexity of the interaction.

Theoretical approaches for the study of quantum many-particle systems naturally begin with the ground-state structure and its energetics. However, quantities that are experimentally more readily accessible are excitation energies and the dynamic structure function. Recent interest in the study of collective excitations[7–11] in finite ^{4}He clusters have been primarily motivated by the need to understand the finite-size dependence of superfluidity[6,9] and the relation between the bulk liquid compressibility and giant resonance energies.[11,12] This has led to the study of vibrational[7–9,11] and rotational[6] collective excitations. Experimentally, the most accessible quantity is the dynamic structure function,[13] which is directly measured by neutron and x-ray scattering in the case of bulk liquid helium and by electron scattering in the case of finite nuclei. The scattering of neutrons off ^{4}He clusters would provide a unique opportunity of directly confronting experimental data with precise first-principles calculations. Finally, since the properties of the excitation spectra contain information on details of the ground-state structure, the theoretical study of excited states also provides valuable feedback on the adequacy of ground-state theories.

In this work, we describe our efforts to understand the zero-temperature ground-state structure of ^{4}He clusters by Monte Carlo methods. More importantly, we show that by directly solving the generalized Feynman eigenvalue equation with inputs of one- and two-body ground-state densities, we not only determine the *optimal* excitation functions and collective excitation energies, but simultaneously obtain a parameter-free dynamic structure function. Further study of sum rules then allows us to determine precisely the collective strength of each state.

The paper is organized as follows: In Sec. II, we discuss existing methods for determining the ground-state structure of ^{4}He clusters. In order to make our paper as complete as possible, we have tried to summarize each method in some detail. In Sec. III, we present ground-state results based on our own variational Monte Carlo (VMC) calculations using Jastrow and triplet trial functions and diffusion Monte Carlo (DMC) calculations using a second-order algorithm. Comparisons are made with other calculations. In Sec. IV, collective excitations are determined via a generalized Feynman eigenvalue equation. Significant differences in excitation energies are observed between calculations, which employ only variational ground-state densities, or density functionals, and those that use exact ground-state densities. The systematic trend of collective energies with cluster size is studied and oscillations in the transition densities are demonstrated. Section V presents results on the dynamic structure function, from which one can readily

identify the cluster excitation spectrum in the continuum. Section VI discusses sum rules and uses them to ascertain, quantitatively, the strength of each collective state. Section VII contains our summary and conclusions.

II. GROUND-STATE METHODS

The ground-state structure of quantum liquid drops can be calculated—in order of increasing degree of sophistication and computational effort—by non-local-density-functional theory, variational Monte Carlo methods, and exact solutions of the many-particle Schrödinger equation. In order to discuss our results in the wider context of what has been done up to now on helium droplets, we will begin with a brief discussion of each available theoretical method for ground-state calculations.

A popular method for the description of nonuniform quantum systems is the density-functional theory.[14] Indeed, for the specific problem at hand, one of the formal problems of density-functional theory[15]—the question of "v representability"—does not occur. In principle, the ground state energy can be written as a functional of the ground state density $\rho_1(\mathbf{r})$

$$E_0 = E_0[\rho_1(\mathbf{r})] \ , \tag{2.1}$$

which is, in turn, obtained by minimizing the energy through the extremum principle:

$$\frac{\delta E_0}{\delta \rho_1(\mathbf{r})} = 0 \ . \tag{2.2}$$

The concrete application of density-functional theory requires the specification of $E[\rho_1(\mathbf{r})]$ in a neighborhood reasonably close to the true ground-state density. Since this information is normally not available, one must resort to approximations. Most common is the *local-density approximation* (LDA). In this approximation, one first writes the total energy as the sum of a kinetic energy $T[\rho_1(\mathbf{r})]$ *plus* a correlation energy $E_c[\rho_1(\mathbf{r})]$:

$$E_0[\rho_1(\mathbf{r})] = T[\rho_1(\mathbf{r})] + E_c[\rho_1(\mathbf{r})] \ . \tag{2.3}$$

$T[\rho_1(\mathbf{r})]$ is the kinetic energy of a weakly interacting model system with the density $\rho_1(\mathbf{r})$; i.e., for the case of a Bose system under consideration here, we have simply

$$T[\rho_1(\mathbf{r})] = \frac{\hbar^2}{2m} \int d^3r \left| \nabla \sqrt{\rho_1(\mathbf{r})} \right|^2 \ . \tag{2.4}$$

The correlation energy is the volume integral of the *correlation energy density* $\varepsilon_c[\rho](\mathbf{r})$,

$$E_c[\rho_1(\mathbf{r})] = \int \varepsilon_c[\rho_1](\mathbf{r}) d^3r \ . \tag{2.5}$$

Then, one approximates the correlation-energy density by the correlation-energy density $\bar{\varepsilon}_c(\rho)$ of the *homogeneous phase*

$$\varepsilon_c[\rho_1](\mathbf{r}) \approx \bar{\varepsilon}_c(\rho_1(\mathbf{r})) \ , \tag{2.6}$$

which is assumed to be a known function of the density. More complicated versions of the density-functional theory—non-local-density approximation (NLDA)—may also include gradient corrections:

$$\varepsilon_c[\rho](\mathbf{r}) \approx \bar{\varepsilon}_c(\rho_1(\mathbf{r}), \nabla \rho_1(\mathbf{r})) \ . \tag{2.7}$$

Of course, one might think of even more complicated non-local dependences of the energy functional on the density, including the exact ground-state theory. To be precise, we will refer to NLDA (LDA) as an energy functional of the form (2.5) with the specific choice (2.6) or (2.7).

The application of the (non-)local-density-functional theory for nonuniform helium liquids encounters both conceptual and physical difficulties: *Conceptually,* the NLDA (LDA) assumes that the uniform phase of the system under consideration exists at all densities under consideration. This is true for electronic systems but not for the helium liquids whose uniform phase exists only to roughly 60% of the equilibrium density.[16] Any local- or non-local-density approximation for the helium liquids therefore implies an extrapolation of the equation of state into an unphysical density regime. *Physically,* the NLDA (LDA) may be thought of as a theory with an effective, density-dependent zero-range interaction. Hence, one can not expect to treat any effect that can be attributed to the existence of a substantial hard core.

Of course, these concerns do not *a priori* preclude that one might obtain some physically reasonable predictions for nonuniform helium liquids from a (non-)local-density-functional theory, and the simplicity of the concept makes the approach quite appealing. In an attempt to use density-functional theory for the calculation of nonuniform helium liquids, Stringari and Treiner[17] suggested a density functional of the form

$$\varepsilon_c(\mathbf{r}) = \frac{1}{2} b[\rho_1(\mathbf{r})]^2 + \frac{1}{2} c[\rho_1(\mathbf{r})]^{2+\gamma} + d|\nabla \rho_1(\mathbf{r})|^2 \ . \tag{2.8}$$

The parameters b, c, and γ are adjusted such that the ground-state energy, density, and compressibility of the homogeneous phase are reproduced. The coefficient d is fixed to account for the experimental surface energy. The inclusion of gradient corrections to the local density functional is quite important. Without such corrections one obtains a surface energy that falls short of the experimental value of 0.274 K Å^{-2} by about a factor of 3.[18] Adding gradient corrections introduces another adjustable parameter, which is used to fit the surface energy. The surface width of the droplets is then also predicted correctly, which lends credibility to the approach. Using the density functional (2.8), it is straightforward to calculate the ground-state structure of a helium droplet.

Microscopic calculations start from a Hamiltonian

$$H = -\frac{\hbar^2}{2m} \sum_i \nabla_i^2 + \sum_{i<j} v(|\mathbf{r}_i - \mathbf{r}_j|) \ , \tag{2.9}$$

where one normally uses the potential derived by Aziz *et al.*[19] for the two-body interaction. A popular approach is to start with a variational ansatz for the ground-state wave function,

$$\phi_0(\mathbf{r}_1,\ldots,\mathbf{r}_N)=\exp\frac{1}{2}\left(\sum_i u_1(\mathbf{r}_i)+\sum_{i<j}u_2(\mathbf{r}_i,\mathbf{r}_j)+\sum_{i<j<k}u_3(\mathbf{r}_i,\mathbf{r}_j,\mathbf{r}_k)\right). \tag{2.10}$$

Roughly speaking, the one-body function $u_1(\mathbf{r})$ impresses the nonuniform structure, the two-body function $u_2(\mathbf{r}_i,\mathbf{r}_j)$ deals with the short-ranged repulsion, and the three-body function $u_3(\mathbf{r}_i,\mathbf{r}_j,\mathbf{r}_k)$ describes triplet correlations. Higher-order correlation functions are, in principle, possible but have not been examined and are most likely negligible. In variational Monte Carlo calculations, one normally employs analytic forms for the correlation functions, which contain a number of free variational parameters. These parameters are fixed by minimizing the ground-state energy. However, when the number of variational parameters proliferates, their optimization is a highly nontrivial and tedious process. (The method of correlated reweighting[20] may help to reduce this effort somewhat.) Moreover, when triplet correlations are included, the required computational effort is comparable to, and may even exceed, that of solving for the ground state exactly. Thus there is a point of diminishing return in pursuing variational Monte Carlo calculations. The other danger of this procedure is that an "educated guess," or limited parametrization of the correlation function, may favor or impose physical orders inappropriate to the system, and one may get out no more than what one has put into the calculation. Due to the stationary character of the lowest eigenvalue, this can still be a useful way of determining the ground-state energy. However, by the same token, good variational energies say very little about how good the variational wave function is. This is especially true when the system has a large number of degrees of freedom. Hence variational calculations of ground-state densities are normally less reliable than the calculation of ground-state energy. We shall return to this important point later on in our discussions.

On the most advanced level, the many-particle Schrödinger equation is solved by the Green's-function[21,22] or the diffusion[23–25] Monte Carlo method. In principle, ground-state properties can be computed with an accuracy that is limited only by the amount of computer time one is willing to invest. In order to properly appreciate the merits of these methods as well as their limitations, it is useful for us to summarize some of their salient features. More details can be found in the above references.

Monte Carlo methods for solving the many-body Schrödinger equation can be regarded as a stochastic means of iterating a *transfer matrix* T such that for n sufficiently large, T^n converges as $T^n \to \text{const}\times\lambda^n\,|\rho\rangle\langle\rho\,|$, where $|\rho\rangle$ is its largest right eigenstate and λ is its largest eigenvalue. In the case of the Green's-function Monte Carlo (GFMC) method, T is the resolvent operator

$$T=(E-z)/(H-z)\ , \tag{2.11}$$

where $H=K+V$ is the many-body Hamiltonian and E, z are convenient constants. In the case of the DMC method, T is the evolution or density-matrix operator,

$$T=e^{-\Delta t(H-E)}\ . \tag{2.12}$$

In both cases, the largest right eigenstate of T is the ground state $|\Psi_0\rangle$ of H with $\lambda_{\text{GFMC}}=(E-z)/(E_0-z)$ and $\lambda_{\text{DMC}}=e^{-\Delta t(E_0-E)}$, from either of which the ground-state energy E_0 can be extracted.

For most applications, the direct iteration of T in the above forms is impractical due to large statistical fluctuations caused by the rapidly varying interparticle potential. As first shown by Kalos, Levesque, and Verlet,[26] significant variance reduction can be achieved with importance sampling using a trial function. Importance sampling can be understood in terms of the transfer matrix as follows:[25] Instead of the original T, one considers an alternative transfer matrix $\tilde{T}$ "similarily transformed" by a trial function Φ_0. For example, in the DMC case, consider instead

$$\tilde{T}=\Phi_0 e^{-\Delta t(H-E)}\Phi_0^{-1}=e^{-\Delta t(\tilde{H}-E)}\ , \tag{2.13}$$

where

$$\tilde{H}\equiv\Phi_0 H\Phi_0^{-1}=\frac{1}{2}\mathbf{p}^2+i\mathbf{p}\cdot\mathbf{G}+E_L(\mathbf{x}) \tag{2.14}$$

is the transformed Hamiltonian, and $G_k(\mathbf{x})=\nabla_k\Phi_0(\mathbf{x})/\Phi_0(\mathbf{x})$. The role of the potential is now played by the local energy $E_L(\mathbf{x})\equiv\Phi_0^{-1}(\mathbf{x})H\Phi_0(\mathbf{x})$, which is generally a much smoother function than the bare potential and causes less fluctuations. In the limit of $\Phi_0(\mathbf{x})\to\Psi_0(\mathbf{x})$, E_L would reduce to a constant equal to the exact ground-state energy and produces no fluctuations at all. Furthermore, although (2.14) is no longer Hermitian, it is apparent that its left and right eigenstates are, respectively, $\langle\Psi_n\,|\Phi_0^{-1}$ and $\Phi_0\,|\Psi_n\rangle$ with unchanged real eigenvalues E_n. Thus with importance sampling, the iteration converges to the product state $\Phi_0\Psi_0$.

In GFMC, since the exact resolvent operator is unknown, it must be sampled by iterating on a simpler, approximate resolvent. In effect, "a Monte Carlo calculation within another Monte Carlo calculation" must be performed. For the DMC method, one can easily sample an approximate evolution operator directly, which is exact in the limit of $\Delta t\to 0$. Second-order algorithms[25] can significantly reduce this step-size error. In both algorithms the product state $\Phi_0\Psi_0$ is evolved, but not Ψ_0^2. To compute the ground-state expectation value of operators other than the Hamiltonian, a simple perturbative estimate is usually invoked,

$$\langle\Psi_0\,|O\,|\Psi_0\rangle=2\langle\Psi_0\,|O\,|\Phi_0\rangle-\langle\Phi_0\,|O\,|\Phi_0\rangle\ . \tag{2.15}$$

Thus, although the ground-state energy can be exactly computed by GFMC or DMC methods, an additional extrapolation error is introduced when computing other ground-state expectation values. The severity of this error can be assessed by using different trial functions to see whether or not one obtains consistent extrapolations. In cases where the trial function is good or when one is dealing with operators not very sensitive to details of the

ground state, this extrapolation error is usually small. However, this cannot be taken for granted. In particular, extrapolation errors are the major source of uncertainties in the computation of ground-state one- and two-body densities defined by

$$\rho_1(\mathbf{r}) = \langle\Psi_0|\sum_i \delta(\mathbf{r}_i - \mathbf{r}_{\text{c.m.}} - \mathbf{r})|\Psi_0\rangle \ , \tag{2.16}$$

$$\rho_2(\mathbf{r},\mathbf{r}') = \langle\Psi_0|\sum_{i\neq j} \delta(\mathbf{r}_i - \mathbf{r}_{\text{c.m.}} - \mathbf{r})\delta(\mathbf{r}_j - \mathbf{r}_{\text{c.m.}} - \mathbf{r}')|\Psi_0\rangle \ . \tag{2.17}$$

This, in turn, affects all calculations based on these densities, such as the determination of collective excitation energies to be described in Sec. III.

III. GROUND-STATE RESULTS

Recent results for the ground-state properties of ^{4}He clusters of size $N = 20$, 40, 70, and 112 are summarized in Table I. We first performed a variational calculation[11] using the following translationally invariant McMillian-type two-body trial function with only two variational parameters,

$$\Phi_0^{\text{I}} = \prod_{i<j} \exp\left(-\frac{1}{2}(a/r_{ij})^5\right) \times \prod_i \exp\left(-\frac{1}{2}b^{-2}(\mathbf{r}_i - \mathbf{r}_{\text{c.m.}})^2\right) \ , \tag{3.1}$$

where $\mathbf{r}_{\text{c.m.}} = (1/N)\sum_{i=1}^N \mathbf{r}_i$. We fixed the parameter a at $a = 3.0$ Å and only adjusted b individually for each cluster size. For the cited particle numbers, optimal values for b are roughly 3.3, 3.6, 3.9, and 4.3 Å, respectively. The resulting ground-state properties are shown in the first row of Table I. The ground-state energy per particle is within 15% of the GFMC or DMC energy, a result that is nearly optimal for a Jastrow-type two-body trial function. Although the percentage difference in the root-mean-square radius $r_{\text{rms}} = \sqrt{\langle r^2\rangle}$ is even smaller (2–4 %), this slight discrepancy causes considerable difficulties in extrapolating ground-state densities. This will be further discussed below. To gauge the adequacy of the trial function for extrapolating the ground-state expectation values via Eq. (2.15), we performed another set of variational calculations with slightly smaller values of 3.2, 3.5, 3.8, and 4.2 Å for b, respectively. The results are shown on the second row. The radii are reduced at the expense of a slight increase of the energy. We next incorporate a triplet correlation in a form suggested by Schmidt *et al.*,[27] which can be derived by suitably simplifying the exact triplet correlation obtained from the three-body Euler-Lagrange equation:[28]

$$\Phi_0^{\text{II}} = \Phi_0^{\text{I}} \exp\left(-\frac{1}{4}\lambda\sum_k \mathbf{G}_k\cdot\mathbf{G}_k + \frac{1}{2}\lambda\sum_{i<j} g^2(r_{ij})r_{ij}^2\right) \ , \tag{3.2}$$

where

$$\mathbf{G}_k = \sum_{l\neq k} g(r_{kl})\mathbf{r}_{kl} \quad \text{and} \quad g(r) = \exp[-(r - r_t)^2/\omega^2] \ . \tag{3.3}$$

The triplet parameters are fixed at $\lambda = -0.9$, $r_t = 1.6$, and $\omega = 1.05$ for all cluster sizes; these values are roughly optimal for $N = 20$. Only the overall size parameter b is again adjusted for each N. The optimal values for b are now systematically smaller: b =3.1, 3.3, 3.6, and 3.9 Å, for N=20, 40, 70, 112, respectively. The corresponding variational energies are within 7–8 % of the exact result, and the rms radii are extremely close to their true values. Our results are given in the third row of Table I. The next row gives the VMC results of Pandharipande, Pieper, and Wiringa[5] using similar triplet correlations. By fine tuning the pair and triplet correlations (totaling 15 parameters); these authors can further reduce the energy discrepancy down to 5%. The results of Krishna and Whaley[9] and their computational efforts are intermediate between ours and those of Pandharipande, Pieper, and Wiringa. Because of the complexity of including triplet

TABLE I. Ground-state properties of ^{4}He clusters as computed by various methods. $\varepsilon_0 = E_0/N$ is the ground-state energy per particle in degrees K; $r_0 = (5/3)^{1/2}\langle r^2\rangle^{1/2}N^{-1/3}$ is the unit radius defined from $\mathbf{r}_{\text{c.m.}}$ in units of Å.

	$N = 20$		$N = 40$		$N = 70$		$N = 112$	
	E_0/N	r_0	E_0/N	r_0	E_0/N	r_0	E_0/N	r_0
VMC-I	−1.447(1)	2.76	−2.196(1)	2.63	−2.744(1)	2.54	−3.143(2)	2.49
	−1.445(2)	2.72	−2.194(1)	2.60	−2.736(2)	2.51	−3.134(1)	2.47
VMC-II	−1.522(2)	2.68	−2.344(1)	2.53	−2.966(1)	2.46	−3.427(2)	2.40
VMC(PPW)[a]	−1.573(1)	2.77	−2.389(2)	2.54	−3.031(3)	2.48	−3.498(5)	2.43
GFMC[b]	−1.627(3)	2.71	−2.487(3)	2.57	−3.12(4)	2.47	−3.60(1)	2.44
DMC-I	−1.650(3)	2.71	−2.525(3)	2.55	−3.188(3)	2.44	−3.702(3)	2.40
	−1.654(3)	2.68	−2.529(3)	2.53	−3.170(2)	2.46	−3.705(3)	2.39
DMC-II	−1.659(3)	2.68	−2.538(4)	2.53	−3.205(4)	2.43	−3.726(4)	2.42
NLDA[c]	−1.27	3.11	−2.18	2.74	−2.93	2.57	−3.51	2.47

[a] Reference 5.
[b] References 3 and 4.
[c] Reference 8.

correlations, the GFMC calculation of Zabolitzky and collaborators[3,4] and our first DMC calculation[11] only use two-body trial functions for importance sampling. Our DMC-I calculation uses the corresponding trial function Φ_0^{I}, Eq. (3.1). The average generation size for both calculations is 200, but, whereas the GFMC calculation iterated about 3500 generations, the DMC-I calculation, which uses a second-order algorithm,[25] iterated 40 000–60 000 generations. The step size used in the DMC-I calculation ranges from Δt=0.002 to 0.0005. With the use of a second-order algorithm, we have checked that doubling or halving the step size has, within statistical fluctuations, no discernible effect on the energy. The two DMC-I entries correspond to two independent calculations using slightly different values of b as described earlier. The GFMC and DMC-I calculations are generally in good agreement; however, the DMC-I energies are systematically about 2% lower than those of GFMC. To further examine the source of this discrepancy, as well as to minimize the extrapolation error in computing the ground-state densities, we performed another DMC calculation, DMC-II, using the triplet trial function Φ_0^{II}, Eq. (3.2), as the importance function. In this case, we limited the number of generation iterated to 10 000–20 000 and lowered the target population for $N = 70$ to 100, but kept the step sizes identical to those of DMC-I. As can be seen from Table I, the agreements between DMC-I and DMC-II results are excellent. Particularly reassuring is the fact that, despite differences in VMC radii, the extrapolated DMC radii are very similar. These agreements not only confirm the convergences of the DMC algorithm, but they also demonstrate its robustness. The algorithm is capable of extracting exact ground-state properties from a rather crude trial function Φ_0^{I}.

For completeness and comparison, we show in the last row of Table I the results of the NLDA calculation by Stringari and Treiner[17] based on the density functional (2.8). For larger clusters, both their energies and radii are in reasonable agreement with GFMC and DMC results. This is expected, since the density functional of Ref. 17 has been fitted such that it reproduces the bulk binding energy, compressibility, saturation density, and surface energy. For small clusters, which are mostly surface, their theory is, as expected, less satisfactory.

The average of all DMC energies and unit radii $r_0 = (5/3)^{1/2}\langle r^2\rangle^{1/2}N^{-1/3}$ over the range of cluster size N=20–112 can be fitted quite accurately by ($x = N^{-1/3}$)

$$\frac{E}{N} = -7.4754 + 21.2729x - 14.8586x^2 \qquad (3.4)$$

and

$$r_0 = 2.1799 + 0.6265x + 1.9935x^2 \ . \qquad (3.5)$$

The extrapolated bulk energy from this fit is −7.4754 K, which is 5% below the experimental value of −7.15 K. It should be pointed out that the extrapolated bulk energy is very sensitive to the order of polynomial used. We also show in Fig. 1 a linear fit that goes through the last two data points. In this case the extrapolated bulk energy is −6.80 K, 5% above the experimental value. If one is to accurately extrapolate the bulk energy from finite

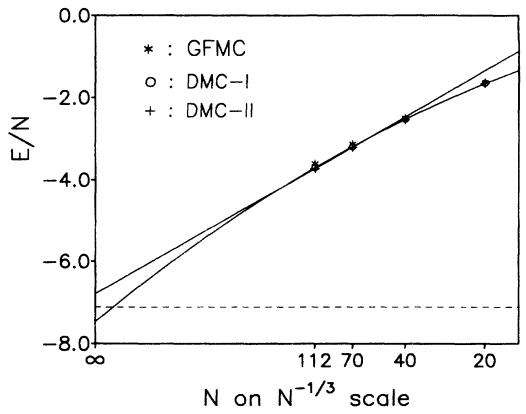

FIG. 1. The ground-state energy per particle as a function of cluster size. The two lines give the linear and the quadratic fits. The dashed line indicates the bulk value.

cluster calculations, heavier clusters must be considered. However, the fact the one can obtain the bulk energy to within 5% from cluster calculations of about 100 particles is in itself quite satisfactory. (The average of the two extrapolated values is, interestingly, −7.14 K.)

Figures 2–5 show the VMC and the DMC one-body densities corresponding to energies quoted in Table I. Again, despite differences in VMC densities, excellent agreement is found among the three DMC calculations, particularly in the outer region of the droplets. While all VMC densities are generally smooth, DMC densities generally show persistent oscillations. In particular, the DMC-I for the $N = 70$ and 112 densities clearly develop a "shoulder" near the surface. It cannot be completely ruled out that these density oscillations are extremely long-lived metastable states that would eventually disappear if iterations were continued far beyond 60 000 generations. On the other hand, the appearance of a geometric shell structure as a consequence of the hard-core-like interaction between the particles is entirely plausible. The dismissal of these density oscillations by mere fiat

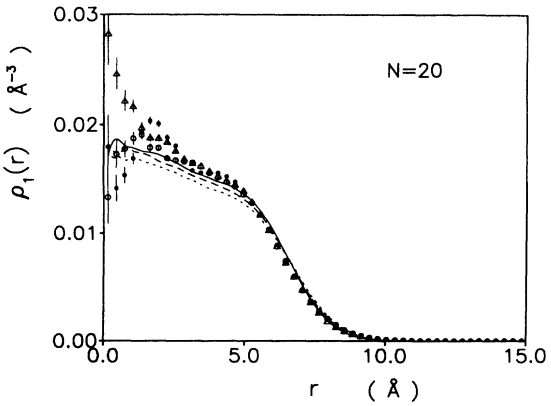

FIG. 2. The one-body density for a $N = 20$ helium cluster. The solid line and solid circles are VMC-II and DMC-II results using triplet trial function Φ_0^{II} (3.2). The two dashed lines and open circles and triangles are two VMC-I and DMC-I results using the two-body trial wave function Φ_0^{I} (3.1).

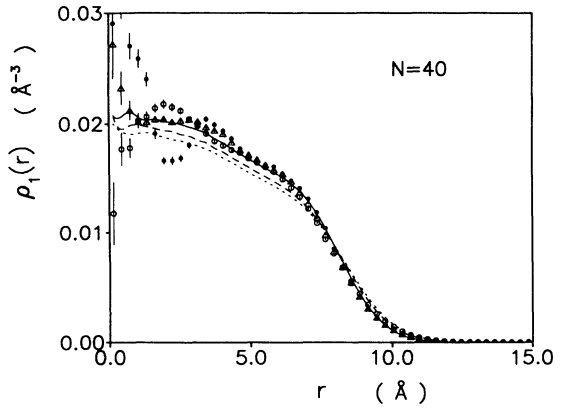

FIG. 3. Same as Fig. 2 for $N = 40$.

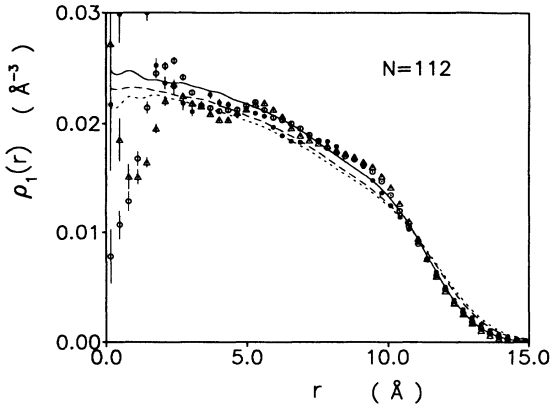

FIG. 5. Same as Fig. 2 for $N = 112$.

is therefore equally groundless. Figure 5 clearly shows that two completely independent DMC-I runs, with different trial functions, yielded similar patterns of oscillation. A pattern of oscillation like that of the $N = 70$ case was also evident in the GFMC calculation[4] using a completely different algorithm. Density oscillations also persisted in our triplet, DMC-II calculations. However, due to the smaller number of iterations, it is difficult to decide whether the pattern of oscillation matches the one of DMC-I. We will come back to the question of density oscillation when we discuss transition densities.

The density-functional and the VMC calculations give reasonable densities profile compared with our DMC calculations. However, they are generally smooth and show no indication of a surface shoulder structure or interior density oscillations. This is hardly surprising since any shell structure of the droplets is a hard-core effect, which is not included in the NDLA. As mentioned earlier, parametrized variational calculations of the ground state can reflect no more structure than what has originally been allowed for in the variational wave function; they therefore have very little to say about these energy-insensitive density oscillations. We expect, however, that *fully optimized* variational calculations of the kind introduced in Ref. 29 would confirm the shell structure of droplets considered here. In passing, we should point out that, since the energy difference per particle between the best VMC calculation[4] with no oscillations and DMC is, at most, 0.2 K, these systematic density oscillations are not expected to be seen in finite temperature calculations[6] at 0.5 K.

Figure 6 compares our VMC and DMC results for the pair-distance distribution $\rho_2(r)$ defined by

$$\rho_2(r) = \int d^3r_1\, d^3r_2 \delta(r - |\mathbf{r}_1 - \mathbf{r}_2|)\rho_2(\mathbf{r}_1, \mathbf{r}_2) \ . \tag{3.6}$$

This function can be obtained with good statistics and is generally smooth. In comparison with DMC results, the triplet wave function $\Phi_0^{\rm II}$ is clearly superior to the two-body Jastrow function $\Phi_0^{\rm I}$. The VMC-II calculation not only gives the correct height for the nearest-neighbor peak, but it also yields a clear next-nearest-neighbor "bump" for the case of $N = 70$ and 112, in agreement with DMC calculations. Again, despite obvious differences in VMC results, excellent agreement is found between the two DMC calculations. In this case, the adequacy of (2.15) for extrapolating ground-state expectation values is amply confirmed. The pair-distance

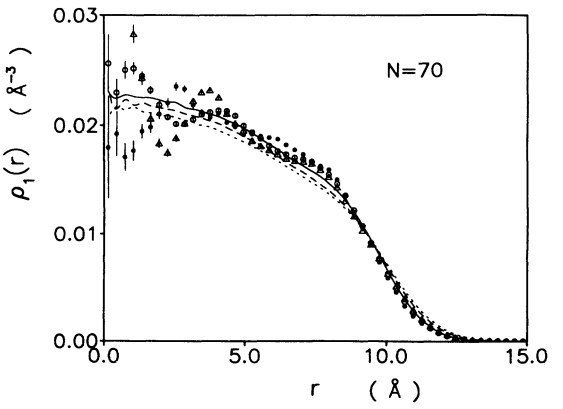

FIG. 4. Same as Fig. 2 for $N = 70$.

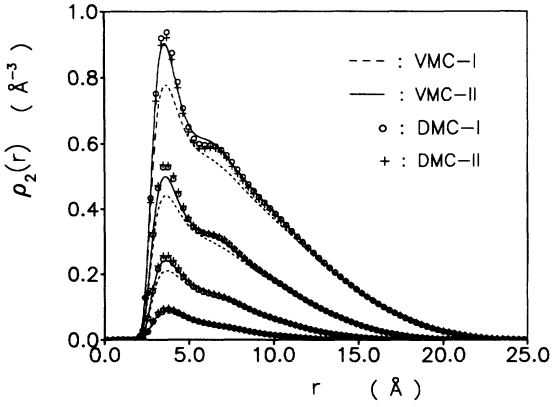

FIG. 6. The pair-distance distribution function as defined by Eq. (3.6) for cluster sizes (from bottom to top) N =20, 40, 70, and 112. The solid line and crosses are VMC-II and DMC-II results using the triplet trial function $\Phi_0^{\rm II}$ (3.2). The dashed line and open circles are VMC-I and DMC-I results using the Jastrow trial wave function $\Phi_0^{\rm I}$ (3.1).

distribution function will be used in Sec. V to compute the static structure and to assess the rate of convergence of the partial wave expansions for excited states.

In binning the two-body density $\rho_2(\mathbf{r}_1, \mathbf{r}_2)$, it is useful and technically advantageous to bin its partial wave amplitudes $\rho_2^{(\ell)}(r, r')$ defined by

$$\rho_2^{(\ell)}(r, r') \equiv \int d\Omega \rho_2(\mathbf{r}, \mathbf{r}') P_\ell(\hat{\mathbf{r}} \cdot \hat{\mathbf{r}}') \ , \tag{3.7}$$

rather than the two-body density itself. The latter would need a three-dimensional binning requiring a huge number of configurations to yield good statistics. When studying collective excitations, one is mostly interested in excitations with low-angular momentum (i.e., monopole and quadrupole excitations). It is then only necessary to compute the partial wave amplitude $\rho_2^{(\ell)}(r, r')$ for small values of ℓ. Thus only a two-dimensional binning of Monte Carlo data is required. Figures 7–12 give the $\ell = 0, 1, 2$ partial wave amplitude in the normalized form of

$$g_\ell(r, r') = \frac{(2\ell + 1)}{4\pi} \frac{\rho_2^{(\ell)}(r, r')}{\rho(r)\rho(r')} \ . \tag{3.8}$$

Figures 7–9 show these amplitudes from a DMC-II calculation for $N = 20$. Figures 10–12 show them for the case of $N = 112$ from a longer DMC-I run. One clearly sees in Fig. 10 that $g_0(r, 0)$ has the expected behavior of a pair-correlation function familiar from bulk liquid helium. The same can also be seen in Fig. 7, but with greater fluctuations.

Due to the less flexible wave function, the VMC-I calculations predict droplets with a slightly lower central density and a slightly larger rms radius. This effect is consistent with the experience from bulk ^{4}He, where Jastrow trial wave functions also predict too low a saturation density of the liquid. In our present application, this effect has a rather discomforting consequence: Because of the larger rms radii of the variational calculations of the ground-state structure, the *extrapolated* DMC-I one-body density [cf. Eq. (2.15)] turns slightly negative at

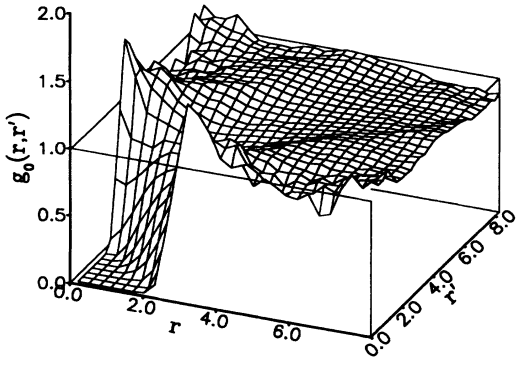

FIG. 7. The DMC-II result for the normalized $\ell = 0$ component of the two-body density as defined by Eq. (3.8) for the case $N = 20$.

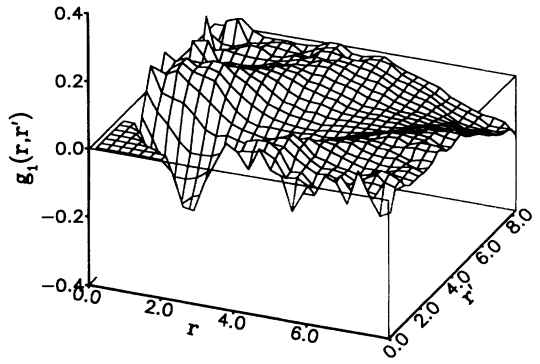

FIG. 8. Same as Fig. 7 for $\ell = 1$.

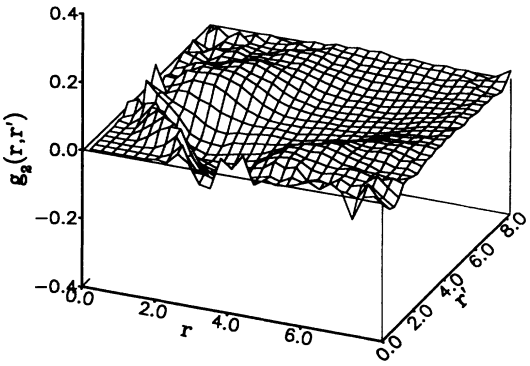

FIG. 9. Same as Fig. 7 for $\ell = 2$.

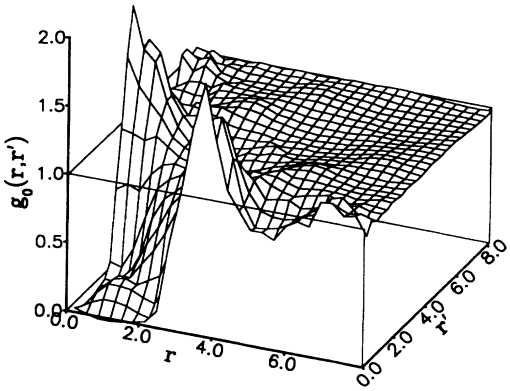

FIG. 10. The DMC-I result for the normalized $\ell = 0$ component of the two-body density as defined by Eq. (3.8) for the case $N = 112$.

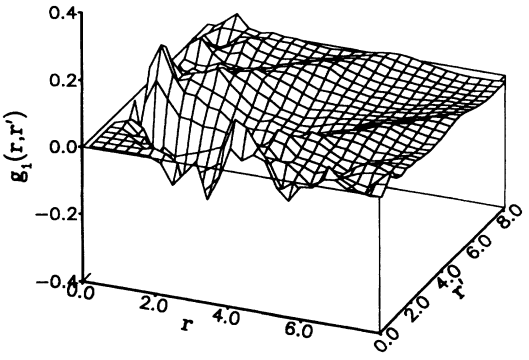

FIG. 11. Same as Fig. 10 for $\ell = 1$.

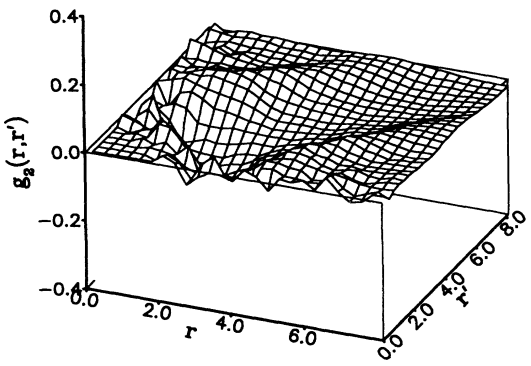

FIG. 12. Same as Fig. 10 for $\ell = 2$.

the very outer edge of the droplet. Since the density at this point is very close to zero, this is usually of little consequence. However, in the calculation of collective excitations, a negative one-body density destroys the positivity of the Hamiltonian describing the collective modes, which is unacceptable. Simply smoothing or setting these negative densities to zero is dangerous because such a procedure will destroy sum rules and sequential relations (see the Appendix) and produce spurious monopole and dipole eigenvalues. To circumvent this problem, we have extrapolated the ground-state distribution functions $g_\ell(r,r')$ directly rather than the pair densities $\rho_2^{(\ell)}(r,r')$. The problem is less severe in the case of DMC-II, where the triplet wave function is a much better trial function and leads to a rms radius that is nearly identical to the exact one. For DMC-II either extrapolation procedure yields essentially the same energy. From this perspective, the triplet trial function Φ_0^{II} has indeed further reduced the extrapolation error.

IV. COLLECTIVE EXCITATIONS

Methods currently available for computing excitation energies of helium clusters can all be interpreted as generalizations of Feynman's theory[30] of collective excitations in liquid ^{4}He. In our work, we assume that we have a translationally invariant solution of the N particle Schrödinger equation, $\Psi_0(\mathbf{r}_1,\ldots,\mathbf{r}_N) = \Psi_0(\mathbf{r}_1+\mathbf{r},\ldots,\mathbf{r}_N+\mathbf{r})$, for example, as evolved by the Monte Carlo methods described in Refs. 3 or 25. Following Feynman, we write a trial function of the excited state as

$$\Psi_F(\mathbf{r}_1,\ldots,\mathbf{r}_N) = F(\mathbf{r}_1,\ldots,\mathbf{r}_N)\Psi_0(\mathbf{r}_1,\ldots,\mathbf{r}_N)\ , \tag{4.1}$$

where

$$F(\mathbf{r}_1,\ldots,\mathbf{r}_N) = \sum_{i=1}^{N}[f(\mathbf{r}_i-\mathbf{r}_{\text{c.m.}}) - \langle f_i\rangle]\ ,$$

$$\langle f_i\rangle = \langle\Psi_0\,|f(\mathbf{r}_i-\mathbf{r}_{\text{c.m.}})\,|\Psi_0\rangle\ . \tag{4.2}$$

Since $\Psi_0(\mathbf{r}_1,\ldots,\mathbf{r}_N)$ is the *exact*, translationally invariant ground-state wave function, the energy difference between the ground state and the trial excited state can be expressed as

$$E_F - E_0 = \frac{1}{2}\frac{\langle\Psi_0\,|[F,[T,F]]\,|\Psi_0\rangle}{\langle\Psi_0\,|F^2\,|\Psi_0\rangle}$$

$$= \frac{\hbar^2}{2m}\frac{(1-1/N)\int d^3r\rho_1(\mathbf{r})|\nabla f(\mathbf{r})|^2 - (1/N)\int d^3rd^3r'\rho_2(\mathbf{r},\mathbf{r}')\nabla f(\mathbf{r})\cdot\nabla f(\mathbf{r}')}{\int d^3r\rho_1(\mathbf{r})|f(\mathbf{r})|^2 + \int d^3rd^3r' f(\mathbf{r})[\rho_2(\mathbf{r},\mathbf{r}')-\rho_1(\mathbf{r})\rho_1(\mathbf{r}')]f(\mathbf{r}')}\ , \tag{4.3}$$

where $E_F = \langle\Psi_F\,|H\,|\Psi_F\rangle/\langle\Psi_F\,|\,\Psi_F\rangle$ is the energy corresponding to the wave function (4.1), and E_0 is the exact ground-state energy. Coordinates in the last line of Eq. (4.3) are measured from the center of mass, and the one- and two-body densities are as defined previously in Eqs. (2.16) and (2.17).

The energy difference $\hbar\omega \equiv E_F - E_0$ determined by Eq. (4.3) is an upper bound to the exact excitation energy. In passing, we note that Eq. (4.3) also results from a variational theory that is based on the wave function (2.10), provided the one- and two-body correlations are determined by the extremum conditions

$$\frac{\delta E}{\delta u_i} = 0 \qquad (i=1,2)\ . \tag{4.4}$$

However, since no variational wave function, even an optimized one, is the exact ground state, the resulting excitation energies are no longer rigorous upper bounds. In particular, if one uses parametrized trial functions for which the global optimization conditions (4.4) are not satisfied, the expression (4.3) will frequently *not* provide reliable estimates of excitation energies.

It is convenient to define $\phi(\mathbf{r}) = \sqrt{\rho_1(\mathbf{r})}f(\mathbf{r})$ so that Eq. (4.3) can be written symmetrically as

$$\hbar\omega = \frac{\int d^3rd^3r'\phi(\mathbf{r})H_1(\mathbf{r},\mathbf{r}')\phi(\mathbf{r}')}{\int d^3rd^3r'\phi(\mathbf{r})S(\mathbf{r},\mathbf{r}')\phi(\mathbf{r}')}\ , \tag{4.5}$$

with the coordinate space representation of the static structure function

$$S(\mathbf{r},\mathbf{r}') = \delta(\mathbf{r}-\mathbf{r}') + \frac{\rho_2(\mathbf{r},\mathbf{r}')-\rho_1(\mathbf{r})\rho_1(\mathbf{r}')}{\sqrt{\rho_1(\mathbf{r})\rho_1(\mathbf{r}')}}\ , \tag{4.6}$$

and the nonlocal kinetic energy operator

$$H_1(\mathbf{r},\mathbf{r}') = -\left(1-\frac{1}{N}\right)\delta(\mathbf{r}-\mathbf{r}')\frac{\hbar^2}{2m}\frac{1}{\sqrt{\rho_1(\mathbf{r})}}\nabla\rho_1(\mathbf{r})\cdot\nabla\frac{1}{\sqrt{\rho_1(\mathbf{r})}} - \frac{\hbar^2}{2mN}\frac{\nabla_{\mathbf{r}}\cdot\nabla'_{\mathbf{r}}\rho_2(\mathbf{r},\mathbf{r}')}{\sqrt{\rho_1(\mathbf{r})}\sqrt{\rho_1(\mathbf{r}')}} \ . \tag{4.7}$$

Calculations of excitation energies differ in the treatment of Eq. (4.5): The *lowest possible* upper bound for the excitation energy is obtained by minimizing the energy difference $\hbar\omega$ with respect to the excitation function $\phi(\mathbf{r})$. This leads to the eigenvalue equation

$$\int d^3r' H_1(\mathbf{r},\mathbf{r}')\phi(\mathbf{r}') = \hbar\omega\int d^3r' S(\mathbf{r},\mathbf{r}')\phi(\mathbf{r}') \ , \tag{4.8}$$

which is the desired generalization of the Feynman dispersion relation.[30] In the limit of the uniform system, one recovers from it the ordinary Feynman spectrum $\omega(k) = \hbar k^2/2mS(k)$. In contrast to the case of bulk liquid helium, the lack of experimental information on the pair distributions for quantum liquid drops precludes the use of Eq. (4.8) to predict the spectra of collective excitations from measurements of the structure function. However, since the pair distribution function can be obtained accurately by an exact solution of the Schrödinger equation, construction of the excited states is just a simple matter of solving the eigenvalue problem (4.8).

Previous excited-state calculations by Wiringa, Pieper, and Pandharipande[7] and Krishna and Whaley[9,10] did not use exact ground-state densities nor the optimal excitation function. Instead, Wiringa, Pieper, and Pandharipande expanded the excitation function in terms of parametrized polynomials and Krishna and Whaley expanded in terms of spherical Bessel functions. By explicitly orthogonalizing these excited states, Krishna and Whaley were also able to estimate some higher-lying excitation energies. Although the connection of the density-functional theory of Casas and Stringari[8] to the Feynman ansatz is less obvious, we will show later that this theory can be interpreted as a zero-range effective interaction theory.

Optimizing the excitation function by exactly solving the eigenvalue problem (4.8) has the significant advantages that one does not need to assume any specific form of the excitation function (as in Ref. 7), the density profile (as in Ref. 9), or the energy functional of the clusters (as in Refs. 8 and 9). Since the excitation functions are eigenfunctions of a generalized Hermitian eigenvalue problem, their orthogonality is guaranteed. In this case, as we shall see, it is rather staightforward to determine higher excitation energies within the Feynman ansatz. Our approach is limited only by (a) the statistical and extrapolation errors in sampling the exact one- and two-body ground-state densities, and (b) the adequacy of the Feynman ansatz, Eqs. (4.1) and (4.2) above.

The eigenvalue problem (4.8) can be decoupled and solved by expanding the excitation function and the two-body density in partial waves,

$$\phi(\mathbf{r}) = \sum_\ell \phi_\ell(r)P_\ell(\hat{\mathbf{r}}\cdot\hat{\mathbf{z}}) \ , \tag{4.9}$$

$$\frac{\rho_2(\mathbf{r},\mathbf{r}')-\rho_1(\mathbf{r})\rho_1(\mathbf{r}')}{\sqrt{\rho_1(\mathbf{r})\rho_1(\mathbf{r}')}} = \sum_\ell \frac{2l+1}{4\pi}h_\ell(r,r')P_\ell(\hat{\mathbf{r}}\cdot\hat{\mathbf{r}}') \ . \tag{4.10}$$

The partial wave expansion of the last term on the right-hand side of Eq. (4.7) is somewhat more complicated. Recalling the definition of $\rho_2^{(\ell)}(r,r')$ from (3.7), one has

$$\rho_2^{(\ell)}(r,r') = \sqrt{\rho(r)\rho(r')}[h_\ell(r,r')+\delta_{\ell,0}] \ . \tag{4.11}$$

The nonlocal term in the one-body operator $H_1(\mathbf{r},\mathbf{r}')$ can then be expanded as

$$\nabla_{\mathbf{r}}\cdot\nabla_{\mathbf{r}'}\rho_2(\mathbf{r},\mathbf{r}') = \sum_\ell \frac{2l+1}{4\pi}d_\ell(r,r')P_\ell(\hat{\mathbf{r}}\cdot\hat{\mathbf{r}}') \ , \tag{4.12}$$

with

$$d_\ell(r,r') = \frac{1}{2\ell+1}\left[\ell(rr')^{\ell-1}\frac{\partial^2}{\partial r\partial r'}\left(\frac{\rho_2^{(\ell-1)}(r,r')}{(rr')^{\ell-1}}\right) + \frac{\ell+1}{(rr')^{\ell+2}}\frac{\partial^2}{\partial r\partial r'}\left[(rr')^{\ell+2}\rho_2^{(\ell+1)}(r,r')\right]\right] \ . \tag{4.13}$$

Both the left- and the right-hand sides of Eq. (4.8) have *two* exact zero-energy eigenfunctions $\phi(\mathbf{r}) = \sqrt{\rho_1(\mathbf{r})}$ and $\phi(\mathbf{r}) = \mathbf{c}\cdot\mathbf{r}\sqrt{\rho_1(\mathbf{r})}$, where $\mathbf{c}$ is an arbitrary constant vector. Neither of these states corresponds to a physical excitation. This is most easily seen by going back to Eqs. (4.2) and (4.3): The first state is a monopole state corresponding to a constant correlation operator; it vanishes identically when the ground-state expectation value is subtracted. The second is a dipole state corresponding to a correlation function $f(\mathbf{r}) = \mathbf{c}\cdot\mathbf{r}$, which describes the translation of the whole droplet. It also vanishes identically due to the translational invariance of the excitation operator: In this case $F(\mathbf{r}_1,\ldots\mathbf{r}_N) = \sum_{i=1}^N f(\mathbf{r}_i - \mathbf{r}_{\text{c.m.}}) = 0$.

It should be clear that it is important for any numerical calculation to maintain these exact properties of the eigenvalue problem (4.8). We show in the Appendix that, in order to guarantee both zero eigenvalues in the partial wave expansion, the sequential relation

$$\int d^3r'[\rho_2(\mathbf{r},\mathbf{r}') - \rho_1(\mathbf{r})\rho_1(\mathbf{r}')] = -\rho_1(\mathbf{r}) \tag{4.14}$$

must be exactly obeyed by the two-body density, *and* $\rho_2(\mathbf{r},\mathbf{r}')$ must be calculated from a translationally invariant wave function satisfying

$$\int d^3r'\,\mathbf{r}\cdot\mathbf{r}'\rho_2(\mathbf{r},\mathbf{r}') = -r^2\rho(\mathbf{r})\ . \tag{4.15}$$

If one or both of these conditions are violated, however slightly, spurious solutions may result. By the nature of Monte Carlo simulations, these two relations are exactly satisfied independent of statistical and extrapolation errors. Thus, for the calculation of excited states, any smoothing of the data must be done very cautiously; otherwise it can do more harm than good.

The center-of-mass correction term in the second line of Eq. (4.7) couples neighboring even and odd multipoles of the two-body density (2.17), cf. Eq. (4.13). We have found, however, that apart from guaranteeing one exact zero eigenvalue in the dipole channel, the effect of these higher-order components is extremely small and can be safely ignored.

Having calculated the excitation function, we obtain finally the (unnormalized) transition density

$$\begin{aligned}\delta\rho_1(\mathbf{r}) &= \int d^3r_1\cdots d^3r_N \sum_i \delta(\mathbf{r}_i - \mathbf{r}_{\text{c.m.}} - \mathbf{r})F(\mathbf{r}_1,\ldots,\mathbf{r}_N)\Psi_0^2(\mathbf{r}_1,\ldots,\mathbf{r}_N)\\ &= \rho_1(\mathbf{r})f(\mathbf{r}) + \int d^3r'[\rho_2(\mathbf{r},\mathbf{r}') - \rho_1(\mathbf{r})\rho_1(\mathbf{r}')]f(\mathbf{r}')\ .\end{aligned} \tag{4.16}$$

The Feynman theory employed here can also be interpreted in terms of a linear-response theory with a *local* particle-hole interaction. The density-density response function is given by the usual random-phase approximation (RPA) relation

$$\chi(\mathbf{r}_1,\mathbf{r}_2;\omega) = \chi_0(\mathbf{r}_1,\mathbf{r}_2;\omega) + \int d^3r_3 d^3r_4 \chi_0(\mathbf{r}_1,\mathbf{r}_3;\omega)V_{\text{p-h}}(\mathbf{r}_3,\mathbf{r}_4)\chi(\mathbf{r}_4,\mathbf{r}_2;\omega)\ , \tag{4.17}$$

where $\chi_0(\mathbf{r}_1,\mathbf{r}_2;\omega)$ is the response function of a "noninteracting" system defined by the one-body Hamiltonian H_1:

$$\chi_0(\mathbf{r}_1,\mathbf{r}_2;\omega) = 2\sqrt{\rho_1(\mathbf{r}_1)}H_1[(\hbar\omega)^2 - H_1^2 + i\eta]^{-1}\sqrt{\rho_1(\mathbf{r}_2)}\ . \tag{4.18}$$

In Eq. (4.17), the local particle-hole interaction is defined as the second variational derivative of the correlation energy functional with respect to the density

$$V_{\text{p-h}}(\mathbf{r}_1,\mathbf{r}_2) \equiv \frac{\delta^2 E_c}{\delta\rho(\mathbf{r}_1)\delta\rho(\mathbf{r}_2)}\ . \tag{4.19}$$

The decomposition of the total ground-state energy into a kinetic energy of the noninteracting system with density $\rho_1(\mathbf{r})$, and "correlation energy" E_c is, of course, well defined only in theories that are based on perturbation theory and/or effective interactions. For example, in the density-functional calculations, Casas and Stringari[8] make the identification

$$V_{\text{p-h}}(\mathbf{r}_1,\mathbf{r}_2) = \left[b + c\left(2+\frac{\gamma}{2}\right)(1+\gamma)\rho^\gamma(\mathbf{r}_1) - \frac{d}{2}(\nabla_1-\nabla_2)^2\right]\delta(\mathbf{r}_1-\mathbf{r}_2)\ . \tag{4.20}$$

This also illustrates our earlier statement that the NLDA can be understood as an effective zero-range theory.

In theories in which the ground state is directly sampled by Monte Carlo methods, the particle-hole interaction no longer plays a central role. The primary two-body quantity of linear response theory is then the two-body density or the pair distribution function. Of course, once a relationship between the pair density and the particle-hole interaction [like the one provided by the RPA relation (4.17)] is established, the one- and two-body densities provide sufficient information to determine this particle-hole interaction. The case of a Bose system is particularly simple, since an algebraic relationship between the static structure function $S(\mathbf{r},\mathbf{r}')$ and the particle-hole interaction $V_{\text{p-h}}(\mathbf{r},\mathbf{r}')$ can be derived.[31]

Using the representation (4.18) of $\chi_0(\mathbf{r},\mathbf{r}';\omega)$, one can formally solve for the full response function $\chi(\mathbf{r},\mathbf{r}';\omega)$:

$$\begin{aligned}\chi(\mathbf{r},\mathbf{r}';\omega) &= 2\sqrt{\rho_1(\mathbf{r})}\{H_1^{\frac{1}{2}}[(\hbar\omega)^2 - H_1^2 - 2H_1^{\frac{1}{2}}\hat{V}_{\text{p-h}}H_1^{\frac{1}{2}} + i\eta]^{-1}H_1^{\frac{1}{2}}\}\sqrt{\rho_1(\mathbf{r}')}\\ &= 2\sqrt{\rho_1(\mathbf{r})}\sum_n (H_1^{\frac{1}{2}}\xi_n)(\mathbf{r})\frac{1}{(\hbar\omega)^2 - (\hbar\omega_n)^2 + i\eta}(H_1^{\frac{1}{2}}\xi_n)(\mathbf{r}')\sqrt{\rho_1(\mathbf{r}')}\ ,\end{aligned} \tag{4.21}$$

where $\hat{V}_{\text{p-h}}(\mathbf{r},\mathbf{r}') \equiv \sqrt{\rho_1(\mathbf{r})}V_{\text{p-h}}(\mathbf{r},\mathbf{r}')\sqrt{\rho_1(\mathbf{r}')}$ and the $\xi_n(\mathbf{r})$ and the $\hbar\omega_n$ are the eigenfunctions and eigenvalues of the problem

$$(H_1^2 + 2H_1^{\frac{1}{2}}\hat{V}_{\text{p-h}}H_1^{\frac{1}{2}})\xi_n = (\hbar\omega_n)^2\xi_n \ . \tag{4.22}$$

From the density-density response function (4.21) one obtains finally the static structure function (4.6)

$$S(\mathbf{r},\mathbf{r}') = -\frac{1}{\sqrt{\rho_1(\mathbf{r})\rho_1(\mathbf{r}')}}\int_{-\infty}^{\infty}\frac{d(\hbar\omega)}{2\pi}\text{Im}\chi(\mathbf{r},\mathbf{r}',\omega)$$
$$= \sum_n \frac{1}{\hbar\omega_n}(H_1^{\frac{1}{2}}\xi_n)(\mathbf{r})(H_1^{\frac{1}{2}}\xi_n)(\mathbf{r}') \ . \tag{4.23}$$

In both Eqs. (4.21) and (4.23), the summation over the frequencies is understood as an integration when the spectrum is continuous. The final step in the analysis is to identify the functions $(H_1^{-\frac{1}{2}}\xi_n)(\mathbf{r})$ with the excitation functions $\phi_n(\mathbf{r})$ introduced in Eq. (4.8). To this end, it is enough to realize that the representation (4.23) of $S(\mathbf{r},\mathbf{r}')$ implies that the functions $(H_1^{-\frac{1}{2}}\xi_n)(\mathbf{r})$ satisfy the eigenvalue problem (4.8); i.e., they are identical to the excitation functions, and the $(H_1^{\frac{1}{2}}\xi)(\mathbf{r})$ are, up to a normalization factor, identical to the transition densities (4.16). This analysis serves to make contact between the method of direct Monte Carlo simulation and the more conventional RPA approach in computing excited states. It will also serve as starting point for the calculation of the full dynamic structure factor $S(k,\omega)$ carried out in the next section.

Having made contact with linear response theory, we turn now to a discussion of our results. The monopole and quadrupole excitation energies for N=20, 40, 70, and 112 particles as obtained by various methods are summarized in Table II. These excitations are *discrete* solutions of Eq. (4.8) with an energy below the threshold for single-particle dissociation, i.e., with energies $\hbar\omega$ satisfying $\hbar\omega + \mu < 0$. From our fitted energy formula (3.4), we obtain for the chemical potential

$$\mu \equiv dE/dN = -7.4754 + 14.1819x - 4.9529x^2 \text{ K} \ . \tag{4.24}$$

For the cluster sizes considered, the chemical potentials are as given in Table II. For reference, the first row gives the liquid-drop model[8] prediction of

$$\hbar\omega_0 = \hbar c\pi/R = 25.6N^{-1/3} \text{ K} \ , \tag{4.25}$$

where the sound velocity is taken to be $\hbar c$ = 18.1 K Å and where $R = 2.22N^{1/3}$ Å is assumed. Using the experimental surface tension of t = 0.27 K Å^{-2}, one also finds that

$$\hbar\omega_2 = 10.4N^{-1/2} \text{ K} \ . \tag{4.26}$$

In the liquid-drop model, all collective monopole modes are unbound. The energy of the collective monopole excitation can be reduced somewhat by using the exact unit radius (>2.22 Å) for each cluster. However, the basic assumption of a sharp surface is simply too crude an approximation for the clusters under discussion. Similarly, the quantized liquid-drop calculation of Krishna and Whaley,[9] which also assumes a sharp surface, gives an unbound energy of $\hbar\omega_0$ = 5.7 K for N = 70. (This is to be distinguished from their Feynman ansatz result quoted in Table II, $\hbar\omega_0$ = 3.90 K.)

The next row gives the RPA results of Casas and Stringari;[8] followed by five entries using the Feynman ansatz but only with variational ground-state wave functions. The calculations of Krishna and Whaley[10] as well as Wiringa, Pieper, and Pandharipande[7] (WPP) use parametrized excitation functions as described previously. Our VMC-I and VMC-II calculations use the optimal excitation function in the sense that the eigenvalue equation (4.8) is solved exactly, but only with input of densities generated by the variational wave function Φ_0^{I} (3.1) and Φ_0^{II} (3.2). The last three rows are results based on extrapolated ground-state densities generated by our DMC simulations.

To appreciate the significance of these results, we plot

TABLE II. Low-lying collective excitations of ^{4}He clusters as computed by various methods. $\hbar\omega_\ell$ is the ℓ-mode collective excitation energy and μ is the chemical potential. Both are given in units of K.

	$N=20$ $\mu=-2.91$		$N=40$ $\mu=-3.67$		$N=70$ $\mu=-4.12$		$N=112$ $\mu=-4.58$	
	$\hbar\omega_0$	$\hbar\omega_2$	$\hbar\omega_0$	$\hbar\omega_2$	$\hbar\omega_0$	$\hbar\omega_2$	$\hbar\omega_0$	$\hbar\omega_2$
LDM[a]	9.43	2.32	7.49	1.64	6.21	1.24	5.31	0.98
CS[a]	2.67				3.90			
KW[b]			3.0	1.4	3.3	1.2	3.4	1.0
WPP[c]	2.85	1.77	2.79	1.72	2.75	1.46	2.63	1.28
VMC-I	2.79	2.03	3.44	1.77	3.38	1.52	2.97	1.27
	2.79	2.14	3.58	1.84	3.53	1.60	3.16	1.34
VMC-II	2.80	2.26	3.68	2.04	3.99	1.77	3.76	1.52
DMC-I	2.72	1.75	3.60	1.37	3.94	1.50	3.92	1.76
	2.72	1.77	3.53	1.50	3.96	1.54	4.27	1.62
DMC-II	2.80	1.71	3.68	1.22	3.97	1.03	4.21	1.20

[a] Reference 8.
[b] Reference 10.
[c] Reference 7.

in Fig. 13 the monopole energy as a function of $N^{-1/3}$. The trend of each calculation is of special interest and is shown by connecting each set of data points by a smooth dotted line. Only the RPA calculation of Casas and Stringari, in which cluster sizes up to $N = 728$ are considered, shows a clear convergence toward the liquid-drop limit. As we go from the Jastrow trial function to the triplet trial function, our VMC monopole energy goes up, in accord with our two DMC calculations. Since our triplet variational results for $N = 20$ and 70 are in good agreement with those of Krishna and Whaley,[10] we extended the dotted line connecting our data onto their result for $N = 240$ ($\hbar\omega_0 = 2.87$ K). The resulting trend line, together with that of VMC-I, gives an excellent impression of how the exact monopole energy must behave: It must initially increase with N and then come down around $N = 112$ and eventually approach the liquid-drop limit. This is physically plausible in that for small N an increase in cluster size increases the interior density and hence raises the speed of sound and hence the monopole energy. For large N, the interior density is already constant; an increase in cluster size simply increases the wavelength of the excitation and therefore lowers the monopole energy. This changeover should occur around cluster sizes such that the central density no longer increases with N. The cluster size $N = 112$ fits such a description perfectly; it is actually also the changeover point of Casas's and Stringari's RPA calculation, although at a lower energy. The scattering of the DMC data at $N = 112$ make this determination less definitive, but future DMC or GFMC calculation at $N = 240$ should resolve this issue.

In view of the good agreement between our triplet calculation and that of Krishna and Whaley, the result of Wiringa, Pieper, and Pandharipande is inexplicable. Their energies are unexpectedly low with no discernible changeover point.

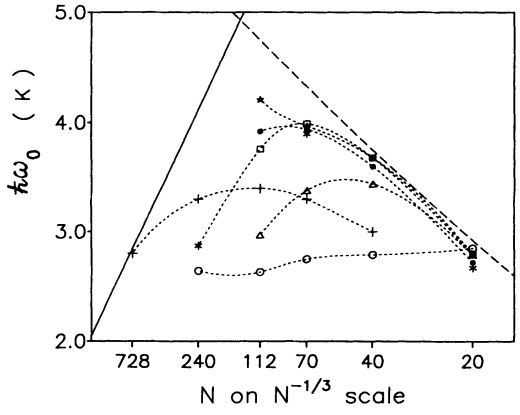

FIG. 13. The monopole collective excitation energy as a function of $N^{-1/3}$. The straight and the dashed lines demarcate the liquid-drop limit, Eq. (4.25), and the chemical potential, Eq. (4.24), respectively. Crosses are the RPA results of Casas and Stringari (Ref. 8). Circles and asterisks are triplet VMC calculations of Wiringa, Pieper, and Pandharipande (Ref. 7) and Krishna and Whaley (Ref. 10), respectively. Our VMC-I and VMC-II results are denoted by triangles and squares and our DMC-I and DMC-II results by dots and stars.

By virtue of its lower energy, the quadrupole is the dominant mode of the cluster excitation. A similar plot of the quadrupole energy is shown in Fig. 14. The first surprise is that all VMC results cross over the liquid-drop line in qualitative disagreement with findings of RPA. Our DMC calculations tend to bring their respective VMC values back down below the liquid-drop line but eventually fail at larger N's. The second surprise is that our triplet wave function not only did not close the gaps between VMC and DMC results; it widens them further. The VMC-II and the DMC-II values can differ by as much as 50%. This is very disconcerting, even though our DMC-II results look reasonable except for the last, $N = 112$ data point. This suggests that although Φ_0^{II} is a clear improvement over Φ_0^{I} in accounting for cluster ground-state energies, one-body densities, pair-distance densities, and the monopole collective energies, at large N it may still be inadequate for describing surface structures, which are important for the quadrupole mode. The fact that the triplet trial function is increasingly inadequate at larger cluster sizes is also clear. At $N = 20$, the difference in total ground-state energy between VMC-II and DMC-II is only about 3 K, comparable to the excitation energies. At $N = 112$, that difference widens to about 30 K, an order of magnitude greater than the excitation energies. Thus to compute the quadrupole energy accurately, one must either further refine the trial function, or adopt other means of extracting exact ground-state densities independent of the trial function.

Despite differences in ground-state trial function and methods of computing excitation energies, the quadrupole energies of WPP and our VMC-I results are in reasonable agreement. However, since these results are not rigorous upper bounds to the excitation energies, and in view of the above discussion, it is difficult to attach much significance to this accord.

Figures 15–18 show our DMC and VMC monopole transition density as given by Eq. (4.16). Systematic oscillations are clearly visible above obvious fluctuations. In the case of $N = 20$, where the triplet wave function

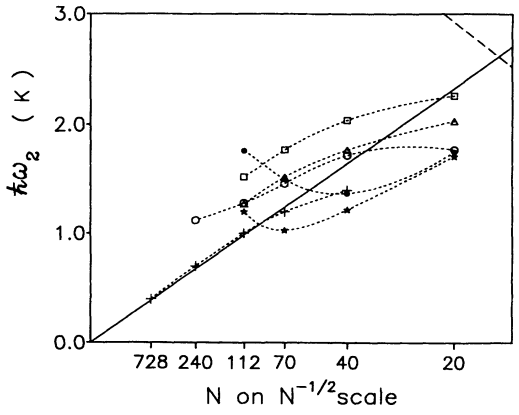

FIG. 14. The quadrupole collective excitation energy as a function of $N^{-1/2}$. Legends are the same as Fig. 13, where results exist. The straight line now gives the liquid-drop limit, Eq. (4.26).

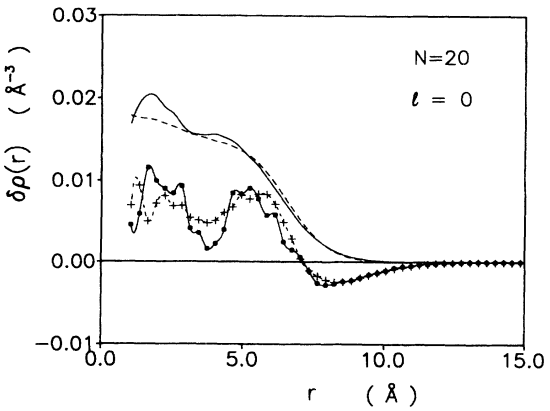

FIG. 15. The monopole transition density for a $N = 20$ helium cluster. The dots and crosses are DMC-II and VMC-II results, respectively. They are connected by smooth and dashed lines to guide the eye. For comparison, their corresponding one-body densities are indicated by a solid and a dashed line. The scale for the transition density is arbitrary; the axis is marked primarily for plotting the one-body density.

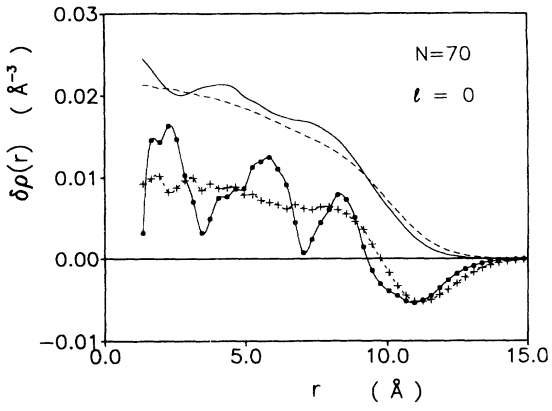

FIG. 17. Same as Fig. 15 for $N = 70$ but with DMC-I and VMC-I results.

Φ_0^{II} is not too bad a ground state, the corresponding variational transition density also shows similar oscillations. As we go to higher N, oscillations in the VMC densities appear to have gone away while those in DMC persist. We have argued previously,[11] on the basis of DMC-I calculations alone (Figs. 17 and 18), that these oscillations, which have wavelengths of the order of 3 Å, are evidence of geometric shell structure connected with the hard-sphere-like interaction between helium atoms. This interpretation is now further strengthened with our triplet calculation for $N = 20$ and 40 (Figs. 15 and 16). The position of the centers of the first two maxima in $N = 20$ and 70 are nearly the same, while those of $N = 40$ and 112 are also similar. It remains to be explained, however, why they do not all agree. It cannot be completely ruled out that these shell-like oscillations are very long-lived metastable states. On the other hand, as in the ground-state density case, we have no basis, theoretical or numerical, for dismissing them *a priori*. Furthermore, they also persist in the quadrupole transition density.

Figures 19–22 show our DMC and VMC quadrupole transition densities. As expected, in all cases, the excitation is concentrated near the surface. For $N = 20$, 40, and 70, where the triplet trial function is used, there is excellent agreement between DMC and VMC results at the outer surface. In the case of $N = 112$, where only the Jastrow function is used, the agreement is markedly poorer. In view of Fig. 14, it is only prudent to consider the DMC-II transition density for $N = 20$, 40, and 70 (Figs. 19–21), for which the corresponding excitation energies have the right trend, as more reliable. However, even in the worst case, that of DMC-I at $N = 112$ (Fig. 22), the transition densities remain qualitatively similar. To see the systematic organization of these oscillations more clearly, we replot Figs. 19–21 as one graph in Fig. 23. The density heights are scaled to be approximately the same and the positions of the $N = 20$ and 40 densities are shifted such that the surface of their one-body density coincides with that of $N = 70$. The two minima are again separated by approximately 3 Å.

It is of obvious interest to study the origin of these oscillations. These may be caused *either* by the oscillations of the bare one-body density, which are amplified by the second derivative of the density appearing in the

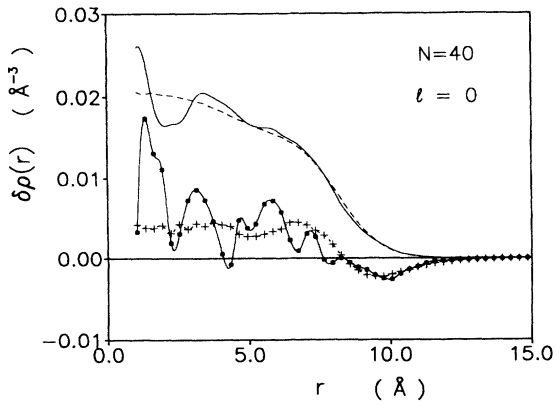

FIG. 16. Same as Fig. 15 for $N = 40$.

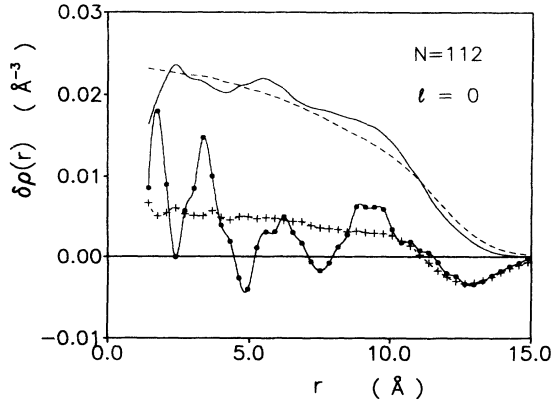

FIG. 18. Same as Fig. 17 for $N = 112$.

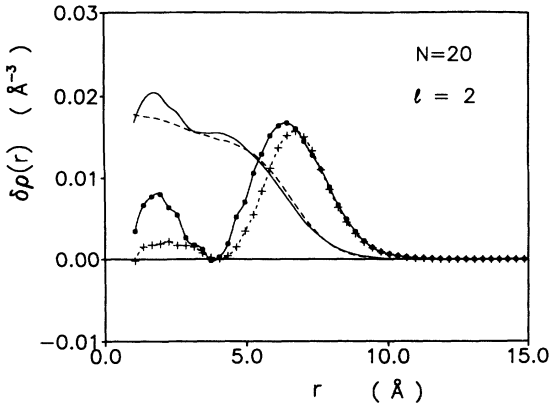

FIG. 19. Same as Fig. 15 but for the quadrupole transition density.

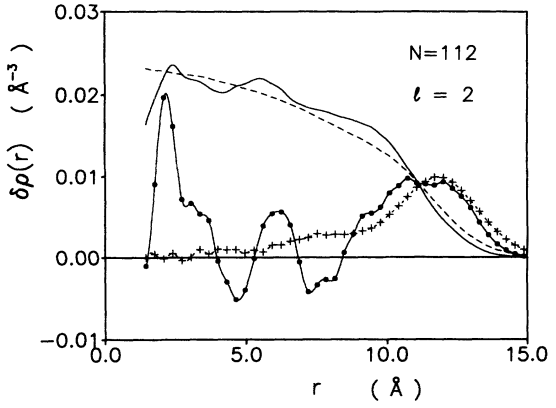

FIG. 22. Same as Fig. 18 but for the quadrupole transition density.

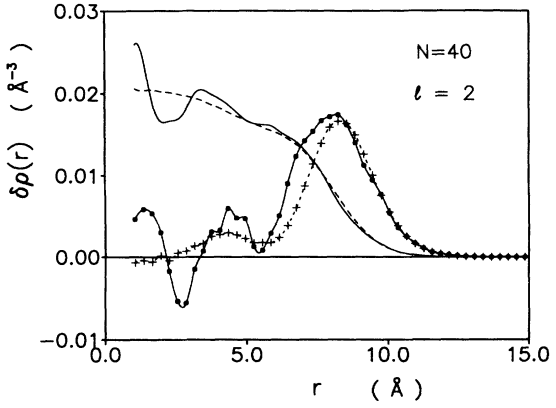

FIG. 20. Same as Fig. 19 for $N = 40$.

one-body Hamiltonian H_1, *or* by the structure of the pair correlations. To decide the issue, we have omitted the pair-correlation function on the right-hand side of Eq. (4.8), i.e., approximated the structure function (4.6) by the first term. This approximation corresponds to the "Hartree-Fock" approximation of Ref. 8. No oscillations of the transition density are seen. We therefore conclude that the shell structure of the transition density is a correlation effect that appears only if the full, nonuniform two-body distribution function is included in the calculation. The analysis also serves as an important accuracy test: A potentially dangerous part of the theory is the calculation of a second derivative of a function that is contaminated by statistical fluctuations. The assurance that such unavoidable uncertainties in the second derivative are not the cause of the fluctuations of the transition density lends further credibility to our results.

Finally, we note that the reality of the oscillations in the transition densities would naturally explain the persistence of oscillations in the ground-state one-body density. These very low-lying excited states would indeed take an extremely long time to decay. In any case, whether it is in the ground-state density or in the tran-

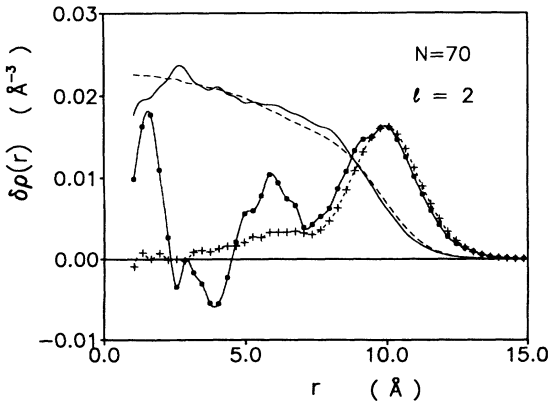

FIG. 21. Same as Fig. 19 for $N = 70$.

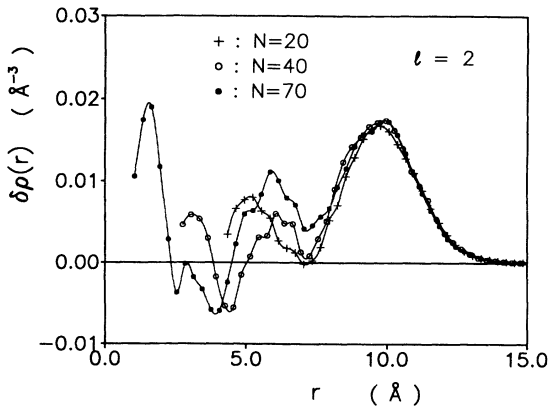

FIG. 23. The DMC-II quadrupole transition density for three cluster sizes.

sition density, these oscillations provide strong evidence for the existence of shell structures in a bosonic quantum system.

V. DYNAMIC STRUCTURE FUNCTION

The excitations of many-body systems such as atoms or nuclei are normally studied by scattering experiments. When the probe is weak, we recall that the scattering cross section is given by the Born approximation by[32]

$$\frac{d^2\sigma}{d\Omega d\omega} = \frac{p_f}{p_i}\left(\frac{d\sigma}{d\Omega}\right)_0 S(\mathbf{k},\omega) , \tag{5.1}$$

where $(d\sigma/d\Omega)_0$ is the differential scattering cross section for scattering from a single constitutent, $\mathbf{p}_i$ and $\mathbf{p}_f$ are the initial and final momenta, $\mathbf{k} = \mathbf{p}_f - \mathbf{p}_i$ is the momentum transfer, and

$$S(\mathbf{k},\omega) = \sum_{n\neq 0} |\langle\Psi_n|\rho(\mathbf{k})|\Psi_0\rangle|^2 \delta(\hbar\omega - E_n + E_0) \tag{5.2}$$

is the dynamic structure function related to the response function by

$$S(\mathbf{k},\omega) = -\frac{1}{\pi}\mathrm{Im}\chi(\mathbf{k},\omega) \qquad (\omega > 0) . \tag{5.3}$$

Inelastic neutron scattering off helium clusters could, in principle, map out the dynamic structure function and allow us to extract excitation energies and transition densities. Theoretically, the calculation of $S(\mathbf{k},\omega)$ requires knowledge of both the excitation spectrum $E_n - E_0$ and the complete set of transition densities $\langle\Psi_n|\rho(\mathbf{k})|\Psi_0\rangle$. As a first step towards an exact calculation of $S(\mathbf{k},\omega)$, to be compared with future experiments, one can replace the exact spectrum and transition densities by those of the Feynman theory, which we have described in the last section.

When the eigenvalue equation (4.8) is discretized on a finite mesh, only a discrete subset of the $\hbar\omega > -\mu$ continuum states is obtained. However, since all functions appearing in the kernels of Eq. (4.8) vanish exponentially for large distances from the center of mass, one can simply extend the mesh to large distances to obtain a very dense spectrum from which reliable information on the density of states can be extracted. We have typically discretized the eigenvalue problem (4.8) in a sphere of 50 Å radius as compared to our droplet radius of about 10 Å. The two-body density $\rho_2(\mathbf{r},\mathbf{r}')$ outside of the sampling region is set to the product $\rho_1(\mathbf{r})\rho_1(\mathbf{r}')$, and the one-body density is extrapolated to large distance by the known asymptotic form $\rho_1(\mathbf{r}) \sim \exp(-2\sqrt{2m\mu/\hbar^2}r)/r^2$. For a given ω, Eq. (4.16) is used to calculate the transition density, from which one obtains a parameter-free model of the dynamic structure function,

$$S(\mathbf{r},\mathbf{r}';\omega) = \delta\rho_\omega(\mathbf{r})\delta\rho_\omega(\mathbf{r}') . \tag{5.4}$$

Adopting our conventions for the weight factors of the partial wave expansion (3.7), and using the same partial wave expansion as in Eq. (4.9) for $\delta\rho_\omega(\mathbf{r})$, we write

$$S(\mathbf{r},\mathbf{r}';\omega) = \sum_\ell \frac{2\ell+1}{4\pi}\delta\rho_{\omega,\ell}(r)\delta\rho_{\omega,\ell}(r')P_\ell(\hat{\mathbf{r}}\cdot\hat{\mathbf{r}}') . \tag{5.5}$$

In momentum-space, we have

$$\begin{aligned} S(\mathbf{k},\mathbf{k}';\omega) &= \int d^3r d^3r' e^{i(\mathbf{k}\cdot\mathbf{r}-\mathbf{k}'\cdot\mathbf{r}')} S(\mathbf{r},\mathbf{r}';\omega) \\ &= \sum_\ell \delta\rho_{\ell\omega}(k)\delta\rho_{\ell\omega}(k')P_\ell(\hat{\mathbf{k}}\cdot\hat{\mathbf{k}}') \equiv \sum_\ell S_\ell(k,k';\omega)P_\ell(\hat{\mathbf{k}}\cdot\hat{\mathbf{k}}') , \end{aligned} \tag{5.6}$$

where $\delta\rho_{\ell,\omega}(k) = \int d^3r \delta\rho_{\ell\omega}(r) j_\ell(kr)$ is the Fourier-Bessel-transform of the transition density corresponding to angular momentum ℓ and energy $\hbar\omega$. The normalization factors relating the transition densities $\rho_\omega(\mathbf{r})$ to the eigenfunctions $\xi_n(\mathbf{r})$ are determined by comparison of the relation

$$\sqrt{\rho_1(\mathbf{r})\rho_1(\mathbf{r}')}S(\mathbf{r},\mathbf{r}') = \int d(\hbar\omega)S(\mathbf{r},\mathbf{r}';\omega) = \sum_{\omega_n+\mu<0} \delta\rho_{\omega_n}(\mathbf{r})\delta\rho_{\omega_n}(\mathbf{r}') + \int_{-\mu}^{\infty} d(\hbar\omega)\delta\rho_\omega(\mathbf{r})\delta\rho_\omega(\mathbf{r}') \tag{5.7}$$

with Eq. (4.23). Discretizing the integral over the continuum states

$$\int_{-\mu}^{\infty} d(\hbar\omega)\delta\rho_\omega(\mathbf{r})\delta\rho_\omega(\mathbf{r}') \approx \sum_{\omega_n} \delta(\hbar\omega_n)\delta\rho_{\omega_n}(\mathbf{r})\delta\rho_{\omega_n}(\mathbf{r}') , \tag{5.8}$$

where $\delta(\hbar\omega_n)$ is the level spacing at the energy value $\hbar\omega_n$, we identify

$$\delta\rho_\omega(\mathbf{r}) = \sqrt{\rho_1(\mathbf{r})}\left(\frac{H_1}{\hbar\omega_n}\right)^{\frac{1}{2}}\xi_n(\mathbf{r}) \tag{5.9}$$

for the discrete states, and

$$\delta\rho_\omega(\mathbf{r}) = \sqrt{\rho_1(\mathbf{r})}\left(\frac{H_1}{\hbar\omega_n\delta(\hbar\omega_n)}\right)^{\frac{1}{2}}\xi_n(\mathbf{r}) \tag{5.10}$$

in the continuum. The corresponding identifications are made in each individual angular momentum channel.

In inclusive scattering experiments, only the diagonal element of $S(\mathbf{k},\mathbf{k}';\omega)$ corresponding to the dynamic structure function is measured:

$$S(\mathbf{k},\omega) = S(\mathbf{k},\mathbf{k};\omega) = \sum_\ell S_\ell(k,k;\omega) , \tag{5.11}$$

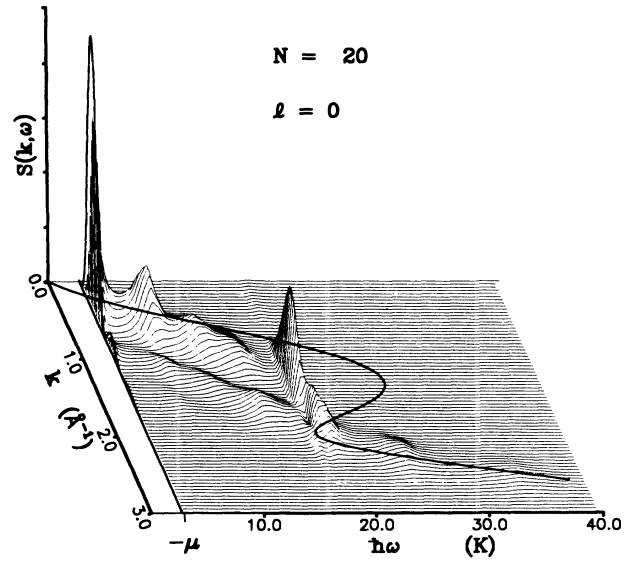

FIG. 24. The ℓ=0 component of the dynamic structure function $S(\mathbf{k},\omega)$ for a $N = 20$ helium cluster. The single line to the left of the continuum gives the strength of the discrete monopole collective mode. The normalization is arbitrary.

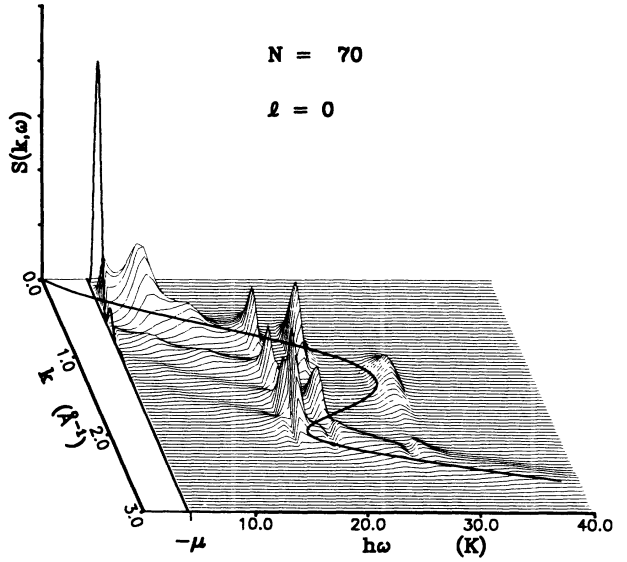

FIG. 26. Same as Fig. 24 for $N = 70$, taken from Ref. 13.

we therefore restrict our investigation to diagonal matrix elements.

Figures 24–27 show plots of our DMC-I calculation of the monopole component of $S_\ell(k,\omega)$. Similar plots of the quadrupole component produced by our DMC-II calculation are shown on Figs. 28–31. For the DMC-II calculation, the statistics are not as good as in the DMC-I case. The monopole and the quadrupole channels each have one *discrete* mode. These states are drawn as lines just left of the continuum in the plots. The overall and relative normalization between the discrete and continuum states is arbitrary. The dipole component is qualitatively similar but without the discrete bound state. For comparison, we draw, in the figures, the Feynman dispersion relation *for bulk liquid helium*. At a fixed value of the excitation energy $\hbar\omega$, the quantity $S(k,\omega)$ is just the square of the Fourier-Bessel transform of the corresponding transition density as a function of k. The overall picture that emerges consists of a series of "ridges" running roughly parallel to the Feynman dispersion curve, punctuated by discrete sets of peaks. As the cluster size becomes larger, these peaks become denser along the Feynman curve, following it with remarkable faithfulness, especially at energies above the roton minimum. The peaks at the maxon and the roton part of the Feynman curve are particularly prominent. The sharply defined peaks that space out at discrete values of $\hbar\omega$ clearly reflect the quantized character of collective excitations appropriate for a finite

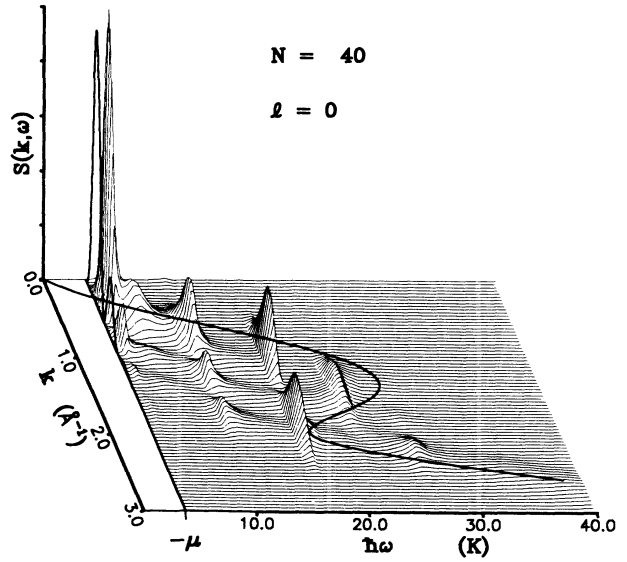

FIG. 25. Same as Fig. 24 for $N = 40$.

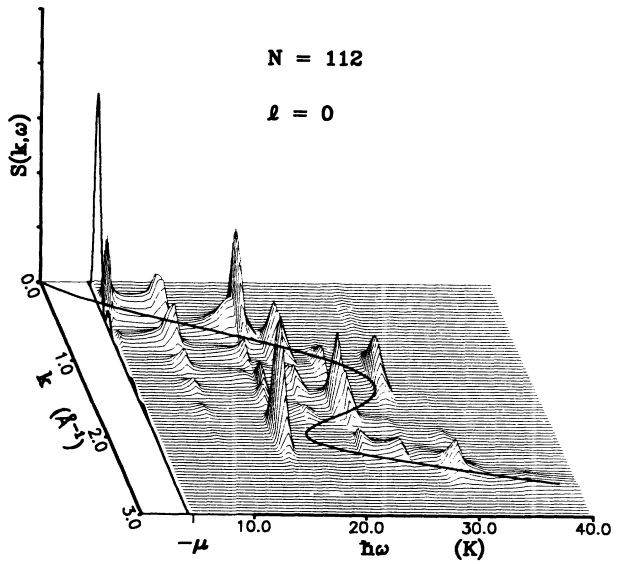

FIG. 27. Same as Fig. 24 for $N = 112$.

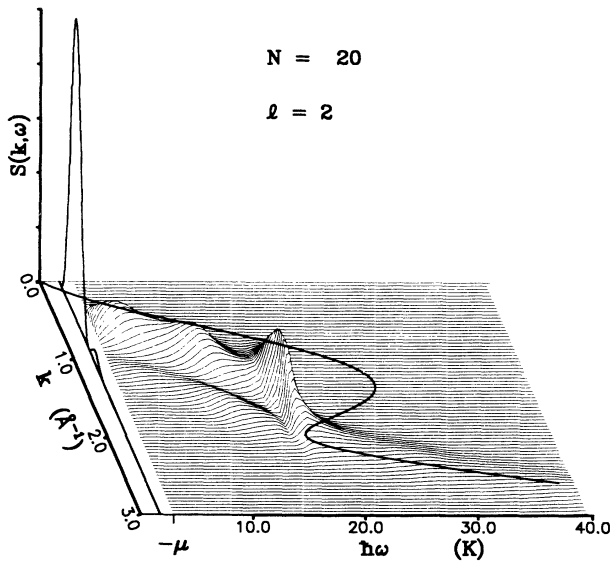

FIG. 28. The $\ell=2$ component of the dynamic structure function $S(\mathbf{k},\omega)$ for a $N = 20$ helium cluster. The single line to the left of the continuum gives the strength of the discrete quadrupole collective mode. The normalization is arbitrary.

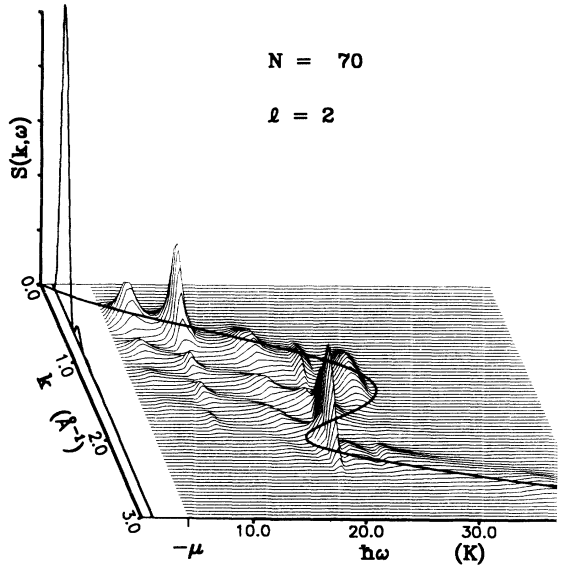

FIG. 30. Same as Fig. 28 for $N = 70$.

droplet. The regular repetition of peaks and ridges along k with diminishing strength appears to be due mostly to "diffractive" effects—this feature arises simply from squaring the Fourier transforms of a transition density which is nonzero only within the droplet. The ridges have the correct spacing in k of roughly π/R, where R is the droplet radius. Obviously, this interpretation does not explain the peak that develops at the roton minimum.

To study the structure of $S(k,\omega)$ in more detail, we show corresponding contour plots in Figs. 32–39. It is now clear that one can directly read off the resonance excitation spectrum of a finite droplet by noting the locations of these scattering peaks. The maxon peak moves up in energy as the cluster gets larger, but seems to be already stabilized at $N = 70$. The phonon part of the peak ridge, originally to the right of the Feynman curve for N, systematically moves left to be centered on the Feynman curve as N increases. The energy spacing between peaks also correctly shrinks with increasing cluster sizes. Thus the dynamic structure-structure function directly maps the cluster excitation spectrum in a very graphic manner and provides a nice picture of how the continuous bulk dispersion relations develop out of the discrete excitation spectra of clusters.

The discrete spectra obtained by orthogonalization in Ref. 9 are in qualitative agreement with our results but differ in details. In particular, the results of Krishna and

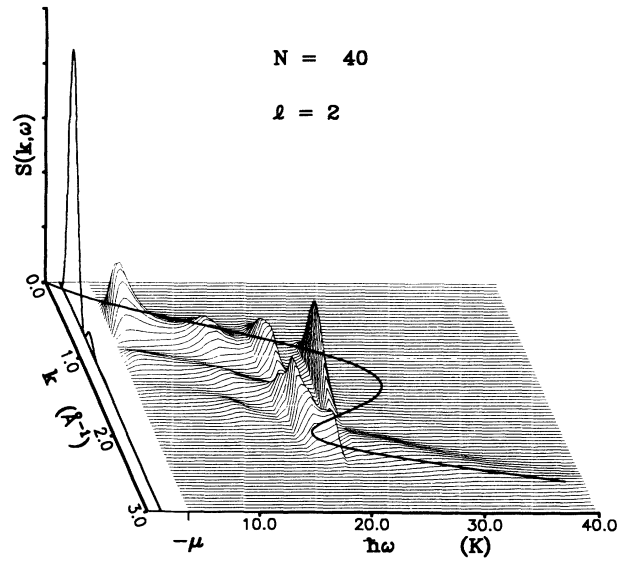

FIG. 29. Same as Fig. 28 for $N = 40$.

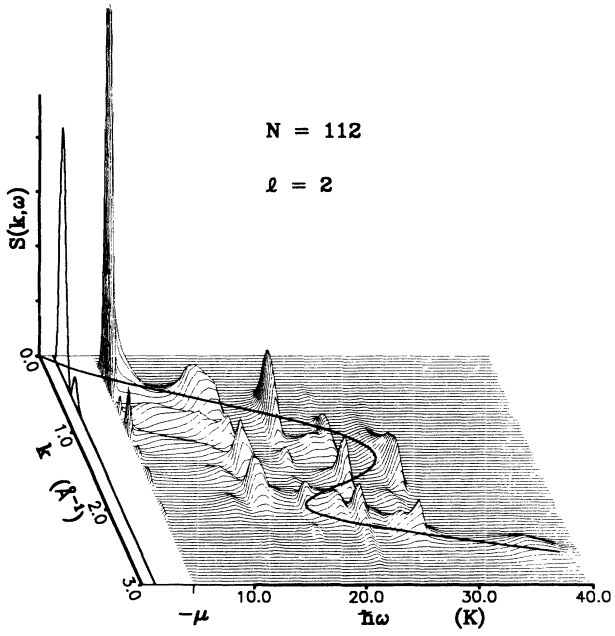

FIG. 31. Same as Fig. 28 for $N = 112$.

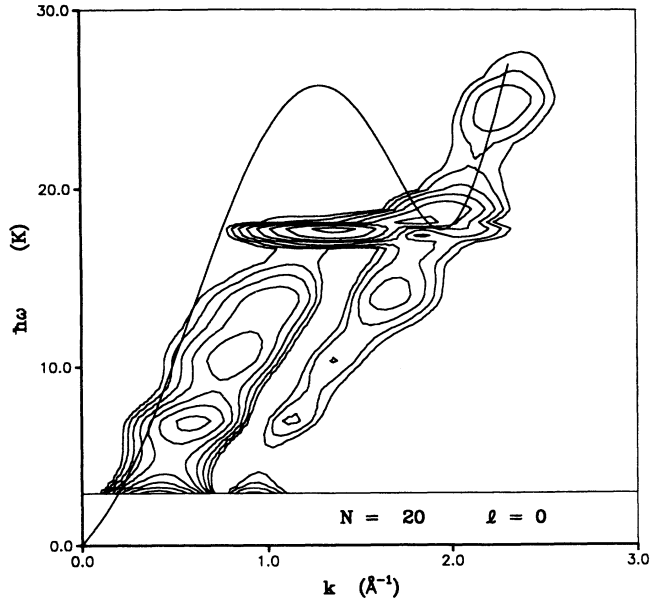

FIG. 32. Contour plot of the ℓ=0 component of the dynamic structure function $S(\mathbf{k},\omega)$ for a $N = 20$ helium cluster. The contour lines depict levels of exponentially varying strength.

Whaley are substantially below ours and the Feynman spectrum near the maxon region for $N \geq 70$.

VI. SUM RULES AND COLLECTIVE STRENGTH

The study of sum rules is useful for understanding particular features of collective states. In general, one considers the nth energy weighted moments

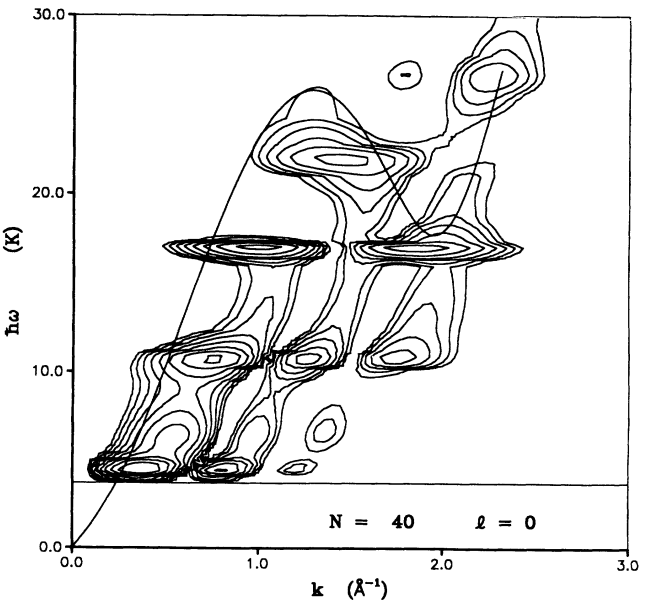

FIG. 33. Same as Fig. 32 for $N = 40$.

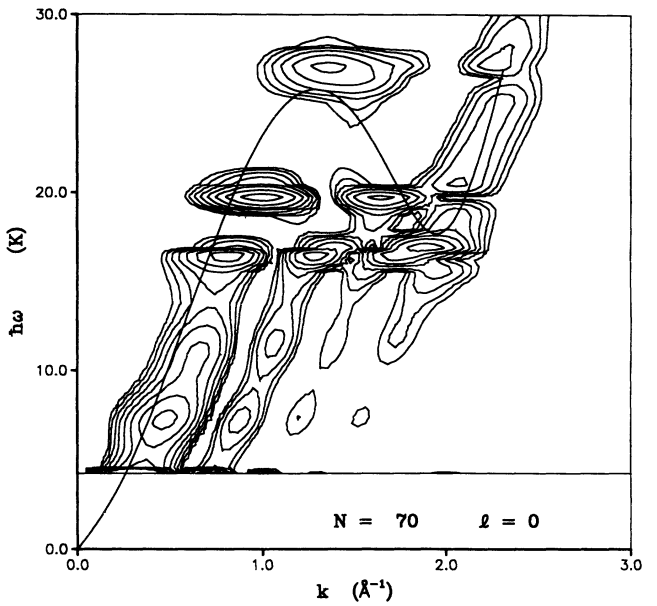

FIG. 34. Same as Fig. 32 for $N = 70$.

$$m_k(r',r) = \sum_{n\neq 0} (E_n - E_0)^k \left\langle \Psi_0 \left| \sum_i \delta(r' - r_i) \right| \Psi_n \right\rangle \times \left\langle \Psi_n \left| \sum_i \delta(r - r_i) \right| \Psi_0 \right\rangle . \quad (6.1)$$

Most of the infinite set of moments $m_n(\mathbf{r},\mathbf{r}')$ cannot be calculated without a specific theoretical model for the density-density response function, for example in the random-phase approximation (4.17). Exceptions are the m_0 and m_1 moments, which are *model independent* in the sense that they require information on the ground-state structure only, in particular,

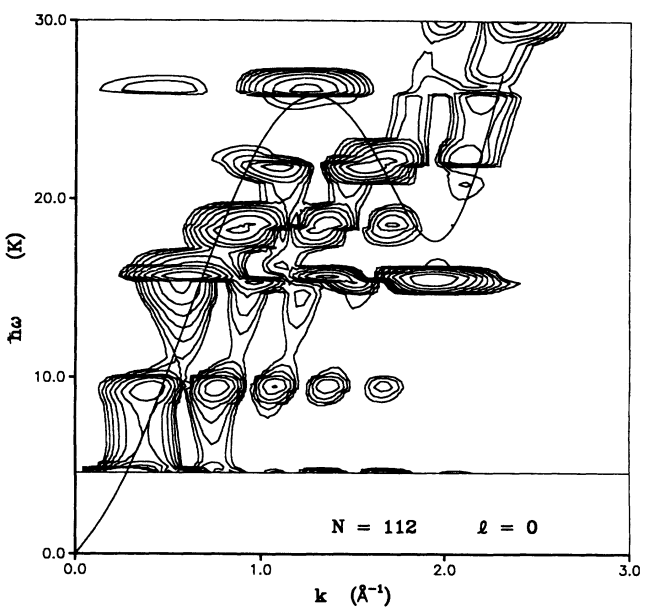

FIG. 35. Same as Fig. 32 for $N = 112$.

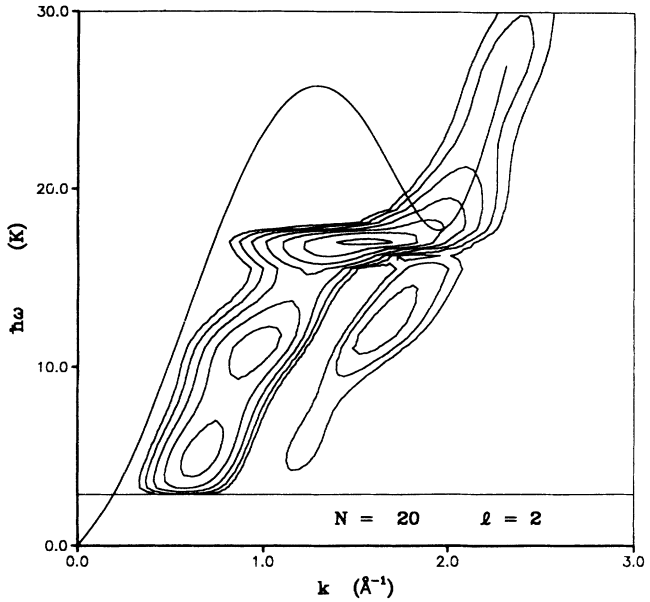

FIG. 36. Contour plot of the $\ell=2$ component of the dynamic structure function $S(\mathbf{k},\omega)$ for a $N = 20$ helium cluster. The contour lines depict levels of exponentially varying strength.

$$m_1(\mathbf{r},\mathbf{r}') = \sqrt{\rho_1(\mathbf{r})}H_1(\mathbf{r},\mathbf{r}')\sqrt{\rho_1(\mathbf{r}')} \tag{6.2}$$

and

$$m_0(\mathbf{r},\mathbf{r}') = \sqrt{\rho_1(\mathbf{r})}S(\mathbf{r},\mathbf{r}')\sqrt{\rho_1(\mathbf{r}')}\ . \tag{6.3}$$

For any trial one-body function $f(\mathbf{r})$, the ratio

$$\frac{m_1[f]}{m_0[f]} \equiv \frac{\int d^3r d^3r' f^*(\mathbf{r}) m_1(\mathbf{r},\mathbf{r}') f(\mathbf{r}')}{\int d^3r d^3r' f^*(\mathbf{r}) m_0(\mathbf{r},\mathbf{r}') f(\mathbf{r}')} \tag{6.4}$$

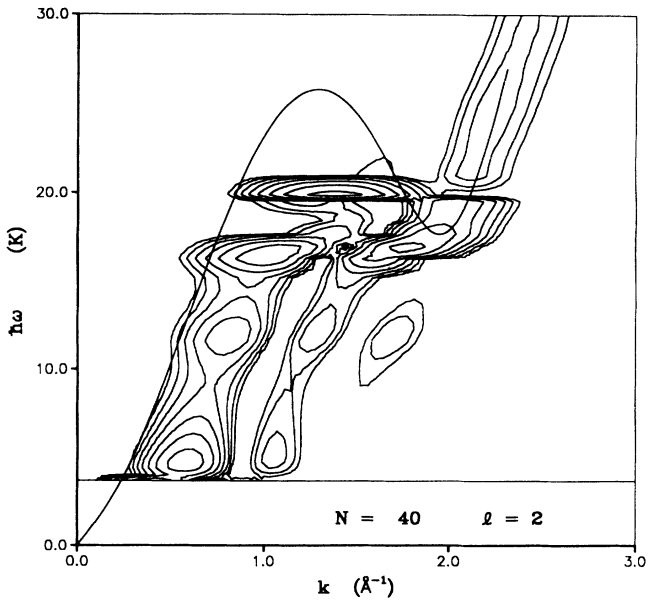

FIG. 37. Same as Fig. 36 for $N = 40$.

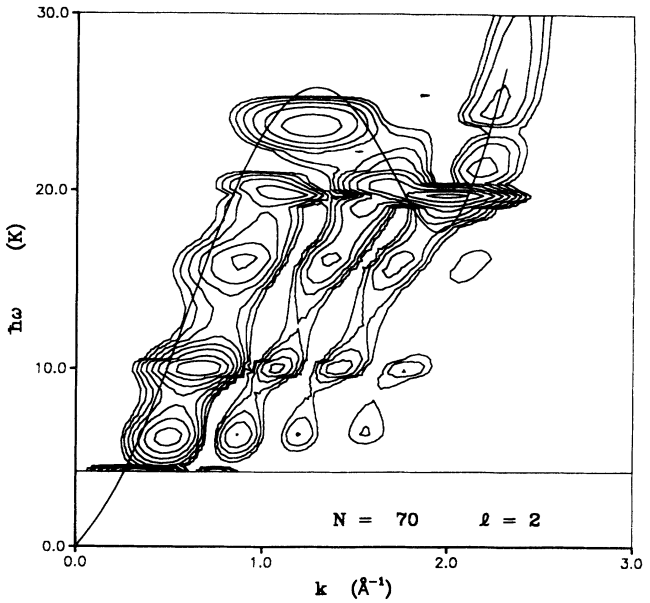

FIG. 38. Same as Fig. 36 for $N = 70$.

is obviously identical to our variational expression (4.5). Thus, $m_1[f]/m_0[f]$ is an upper bound for the excitation energy of the lowest-lying collective mode with the symmetry of the excitation function:

$$\frac{m_1[f]}{m_0[f]} \geq \hbar\omega_0\ . \tag{6.5}$$

Other sum rules like m_3 or m_{-1} depend on the specific model of the response function. Our theory of the excited states implies the random-phase approximation. Hence, there are only two independent quantities, namely, $H_1(\mathbf{r},\mathbf{r}')$ and $S(\mathbf{r},\mathbf{r}')$, and the other sum rules provide no additional information.

Sum rules may be utilized in two different ways: One

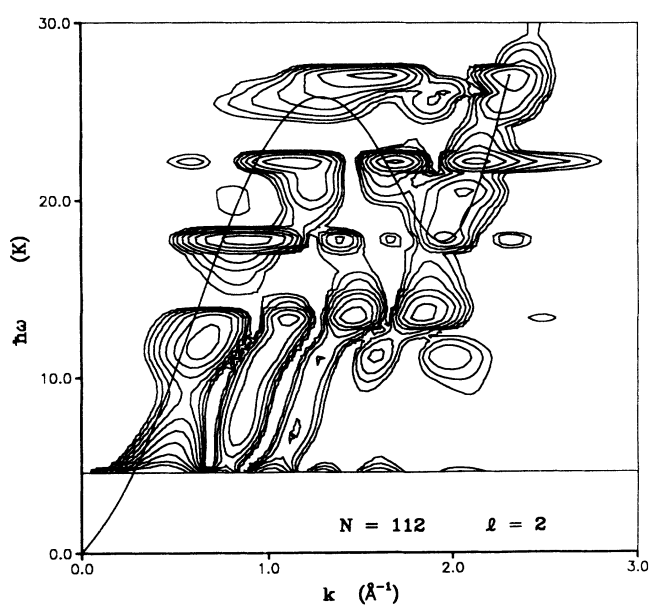

FIG. 39. Same as Fig. 36 for $N = 112$.

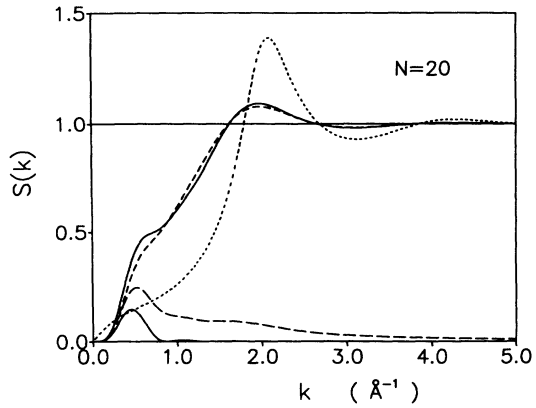

FIG. 40. Sum rule results for cluster size $N = 20$. The solid line is the cluster static structure function computed with DMC-II densities according to Eq. (6.8). For comparison, the short-dashed line is the triplet variational structure function computed with VMC-II densities. The dotted line is the experimental bulk helium structure function. The contribution to $S(k)$ from the quadrupole collective state is given by the solid hump. The sum of contributions from all states in the three lowest angular momentum modes is given by the long-dashed line.

is to use the inequality (6.5) to estimate low-lying excitation energies from an "intelligent guess" of the excitation operator $f(\mathbf{r})$. We have determined the excitation operator optimally by exactly minimizing the ratio $m_1[f]/m_0[f]$ with respect to $f(\mathbf{r})$. The other use of sum-rules is to analyze the contribution of specific excitations to the full static structure function $S(k)$ and to determine which collective state will be most likely excited by an external probe. In that case, the function $f(\mathbf{r})$ describes the external probe. Since such a probe will normally be a plane wave, we work in momentum space and consider, as in the preceding section, only diagonal matrix elements. In other words, we use the excitation operator $f(\mathbf{r}) = \exp(i\mathbf{k}\cdot\mathbf{r})$.

For finite systems, sum rules can be discussed on two levels. First, we can study sum rules in each individual angular-momentum channel. This will give information on the relative strength of a specific excited state as compared with the total excitation strength in a given angular momentum channel. For our purpose, we are most interested in the monopole and the quadrupole channel. For this study, we can directly compute the angular momentum components of the static structure function by Fourier transforming $S(\mathbf{r},\mathbf{r}')$ [cf. Eq. (4.6)]

$$S_\ell(k) = \frac{1}{N}\int d^3r d^3r' \sqrt{\rho_1(\mathbf{r})\rho_1(\mathbf{r}')}e^{i\mathbf{k}\cdot(\mathbf{r}-\mathbf{r}')} \times S(\mathbf{r},\mathbf{r}')P_\ell(\hat{\mathbf{r}}\cdot\hat{\mathbf{r}}') , \tag{6.6}$$

and compare with the result of integrating the dynamic structure function

$$S_\ell(k) = \frac{1}{N}\int_0^\infty d(\hbar\omega)S_\ell(k,\omega) = \frac{1}{N}\int_0^\infty d(\hbar\omega)|\delta\rho_{\omega,\ell}(k)|^2 . \tag{6.7}$$

When solving the eigenvalue problem (4.8) on a finite mesh, these two methods of calculating $S_\ell(k)$ provide an excellent check on the numerics of computing excitation energies and transition densities.

On the other level, we can study the contribution of the individual angular-momentum components to the total static structure function $S(k)$. This study provides independent information, since $S(k)$ can be calculated directly from the pair-distance distribution (3.6):

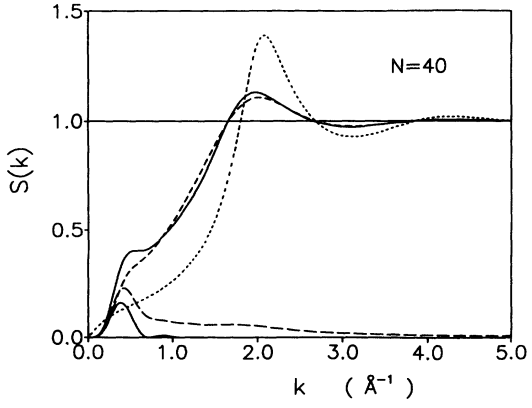

FIG. 41. Same as Fig. 40 for $N = 40$.

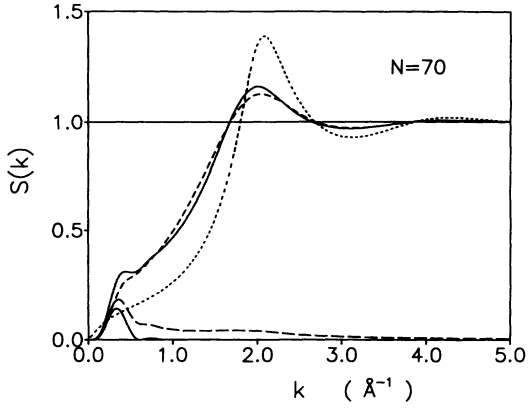

FIG. 42. Same as Fig. 40 for $N = 70$.

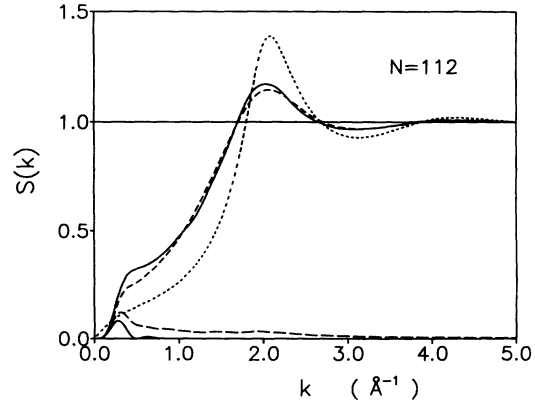

FIG. 43. Same as Fig. 40 for $N = 112$.

$$S(k) = \sum_{\ell} S_{\ell}(k)$$
$$= \frac{1}{N} \int d^3r d^3r' \sqrt{\rho_1(\mathbf{r})\rho_1(\mathbf{r}')} e^{i\mathbf{k}\cdot(\mathbf{r}-\mathbf{r}')} S(\mathbf{r},\mathbf{r}')$$
$$= 1 + \frac{1}{N}[\tilde{\rho}_2(k) - |\tilde{\rho}_1(k)|^2] , \quad (6.8)$$

where $\tilde{\rho}_2(k)$ and $\tilde{\rho}_1(k)$ are Fourier transforms of the pair-distance and one-body densities, respectively. Since the last line of Eq. (6.8) can be evaluated without the use of a partial wave expansion, we have an independent test on the convergence rate of the partial wave expansion. We also can make statements regarding the probability with which individual angular momentum channels are excited by a plane wave probe.

For the four cluster sizes considered, Figs. 40–43 show comparisons between calculated droplet structure functions $S(k)$, the static structure function of bulk ^{4}He at saturation density, and contributions from the individual angular momentum components and collective modes. These four figures exhibit two remarkable features: One is the greatly reduced overshoot of the droplet $S(k)$ around $k \approx 2$ Å^{-1}, and the other one is the shoulder around $k \approx 0.5$ Å^{-1}, which is absent in the bulk $S(k)$. In connection with the overshoot reduction, around $k \approx 2$ Å^{-1}, we recall that the resonances discussed in the preceding section follow faithfully the Feynman dispersion curve

$$\hbar\omega(k) \approx \frac{\hbar^2 k^2}{2mS(k)} , \quad (6.9)$$

where the *bulk* $S(k)$ is used. Taking the droplet $S(k)$ instead in the same relationship would yield a much shallower "roton minimum." Thus it is clear that these continuum excitations of the system are, at these wavelengths, considerably influenced by short-ranged correlations, whereas the full cluster $S(k)$ reflects much more of averaged properties.

The long-dashed line in Figs. 40–43 represent the sum of all contributions to $S(k)$ originating from the first three angular-momentum components, including that of the collective quadrupole excitation. It appears that the collective quadrupole is by far the largest single contributor to the full $S(k)$ and is mainly responsible for the shoulder observed at $k \approx 0.5$ Å. This shoulder was observed previously in the calculation of Schiavilla *et al.*[33] However, they did not propose any explanation for its presence. The quadrupole accounts for more than half of the total strength in the first three angular-momentum states and amounts to 25–30 % of the overall excitation strength. By contrast, the monopole's contribution is negligible (< 5%).

VII. SUMMARY AND CONCLUSIONS

Helium clusters are unique bosonic systems of great intrinsic interest. Because of the relatively simple ^{4}He-^{4}He interaction, they are also excellent laboratories for testing our theoretical understanding of finite quantum many-body systems. With the advent of supercomputers, we have in our grasp unprecedented raw computational power for understanding the physics of clusters from first principles. What is needed, however, are theoretical methods and efficient algorithms that can harness this power for the extraction of physical results. We have presented in this paper microscopic methods for computing ground-state properties and excitation spectra of any finite bosonic quantum systems and have applied them with great success in elucidating the properties of helium droplets. In summary, we have (1) computed the exact ground-state energies of helium clusters using a second-order DMC algorithm with triplet trial functions (the cluster energies are lower than any previous Monte Carlo simulation and extrapolate correctly to the experimental bulk energy at infinite cluster size), (2) exactly solved the generalized Feynman eigenvalue equation, which optimally determines the one-body excitation operator and collective excitation energies, (3) determined the systematic variation of collective energies with cluster size and shown how the liquid-drop limit is approached, (4) demonstrated the existence of systematic density oscillation in transition densities, which strongly suggest the possible existence of geometric shell structure in helium clusters, (5) computed the cluster dynamic structure from which the entire cluster excitation spectrum can be identified, (6) demonstrated in detail how the continuous bulk phonon-roton spectrum may have emerged from the discrete cluster resonance spectrum, and (7) quantitatively determined the strength of each collective state from the static structure function by use of sum rules and identified the quadrupole as the dominant collective mode for clusters with size $N \lesssim 100$.

One of the major conclusions of our work is that a great deal of physics can be extracted from knowing just the one- and two-body ground-state densities. However, the binning of two-body densities requires an order of magnitude more computer time than that of one-body densities. By comparison, the mere evaluation of ground-state energies seems trivial. Moreover, the extraction of exact one- and two-body densities is hampered by perturbative extrapolation errors that are too dependent on the quality of the trial function. Most serious is the fact that the perturbative estimate Eq. (2.15), although it respects sum rules, does not guarantee the positivity of densities. A better method for obtaining the exact ground-state densities would be most helpful. (For some recent suggestions, see Barnett, Reynolds, and Lester.[34])

In computing the excited states, we have found unexpected oscillations in the transition density for the monopole and quadrupole excitation, which are evidently related to the geometric shell structure of clusters due to the hard-core-like interaction of ^{4}He atoms. The fact that these are very low-energy excitations is also consistent with the observed persistent oscillations in the ground state one-body densities. Our analysis of the dynamic structure function provides a physically plausible and appealing picture of the transition from small clusters, whose excitations can be best regarded as being a discrete series of collective modes and resonances, to large clusters, whose excitations are essentially continuous and follow the phonon-roton curve. Our analysis

of the sum rules and the angular momentum decomposition of the static structure function revealed that the only discrete excitation with a significant strength is the collective quadrupole mode.

Althrough our calculation of the dynamic structure function provides a physically appealing scenario of the transition from pronounced discrete excited states of a small system to a basically continuous spectrum of a large system, it is well known that the Feynman spectrum for bulk ^{4}He in the regime of the maxon and/or roton is only qualitatively correct. Quantitative uncertainties implicit in the Feynman ansatz for finite clusters are presently unknown. For very large droplets they should be of the same order magnitude as the inaccuracies of the Bijl-Feynman dispersion relation for bulk liquid. However, nothing is known for smaller systems. The reduced peak in the static structure function may hint towards a less pronounced roton minimum and perhaps less important corrections to the Feynman spectrum. But the accuracy of our predictions cannot be determined within the theory. The next step would involve the introduction of two-body correlations in the excitation function (4.2). This would require the sampling of three- and four-body correlation functions, which is presently computationally too demanding. A rather accurate estimate of the importance of multiple-phonon processes can be obtained by correlated-basis-function perturbation theory using the Feynman density fluctuations as a basis.[35]

ACKNOWLEDGMENTS

This work was supported, in part, by the National Science Foundation under Grant Nos. PHY89-07986 (to S.A.C.) and PHY-8806265 (to E.K.), and the Texas Advanced Research Program under Grant No. 010366-012 (to E.K.). The simulations of the ground-state structure were performed on the CRAY-YMP of the Texas A&M University Supercomputer Center. One of us (E.K.) thanks the Minnesota Supercomputer Institute and the Theoretical Physics Institute at the University of Minnesota where a part of this work was carried out, for warm hospitality and support. Our paper profited from discussions with C. E. Campbell and J. W. Clark, and by numerous suggestions on the manuscript by J. W. Clark.

APPENDIX

In this appendix we show how the existence of two zero-frequency solutions of the eigenvalue problem is verified in the partial wave expansion. A check of these exact properties provide a valuable test for the numerical accuracy of the calculation and, in particular, on the statistical errors inherent to the Monte Carlo simulation of the distribution functions. In the monopole channel, we have

$$d_0(r,r') = \frac{1}{(rr')^2}\frac{\partial^2}{\partial r\partial r'}\left[(rr')^2\rho_2^{(1)}(r,r')\right] \tag{A1}$$

and hence

$$\int dr'r'^2\frac{d_0(r,r')}{\sqrt{\rho_1(r)\rho_1(r')}}\sqrt{\rho(r')} = \frac{1}{r^2\sqrt{\rho_2^{(1)}(r)}}\frac{d}{dr}\int dr'\frac{\partial}{\partial r'}\rho_2^{(1)}(r,r') = 0 . \tag{A2}$$

The right-hand side of Eq. (4.8) vanishes due to the sequential relation (4.14). In the dipole channel, we have

$$d_1(r,r') = \frac{1}{3}\left(\frac{\partial^2\rho_2^{(0)}(r,r')}{\partial r\partial r'} + \frac{2}{(rr')^3}\frac{\partial^2}{\partial r\partial r'}[(rr')^3\rho_2^{(2)}(r,r')]\right) . \tag{A3}$$

The excitation function $\phi_1(\mathbf{r}) = \mathbf{c}\cdot\mathbf{r}\sqrt{\rho_1(\mathbf{r})}$ corresponds to a dipole excitation $\phi_1(r) = r\sqrt{\rho_1(r)}$ and

$$\int dr'r'^2\frac{d_1(r,r')}{\sqrt{\rho_1(r)\rho_1(r')}}r'\sqrt{\rho_1(r')} = \frac{1}{3\sqrt{\rho_1(r)}}\frac{d}{dr}\int dr'r'^3\frac{\partial}{\partial r'}\rho_2^{(0)}(r,r') = 2\frac{d}{dr}\sqrt{\rho_1(r)} , \tag{A4}$$

which is easily seen to cancel the local part of $H_1(\mathbf{r},\mathbf{r}')$ in the dipole channel. In the last line of Eq. (A4), we have again used the sequential relation (4.14).

The right-hand side is also zero for the same function. To prove this, consider

$$\begin{aligned}\int d^3r'\mathbf{r}\cdot\mathbf{r}'\rho_2(\mathbf{r},\mathbf{r}') &= \int d^3r'\mathbf{r}\cdot\mathbf{r}'\left\langle\Psi_0\left|\sum_{i\neq j}\delta(\mathbf{r}_i-\mathbf{r}_{\text{c.m.}}-\mathbf{r})\delta(\mathbf{r}_j-\mathbf{r}_{\text{c.m.}}-\mathbf{r}')\right|\Psi_0\right\rangle \\ &= \int d^3r'\left\langle\Psi_0\left|\sum_{i\neq j}\mathbf{r}\cdot(\mathbf{r}_j-\mathbf{r}_{\text{c.m.}})\delta(\mathbf{r}_i-\mathbf{r}_{\text{c.m.}}-\mathbf{r})\delta(\mathbf{r}_j-\mathbf{r}_{\text{c.m.}}-\mathbf{r}')\right|\Psi_0\right\rangle \\ &= \int d^3r'\left\langle\Psi_0\left|\sum_{i,j}\mathbf{r}\cdot(\mathbf{r}_j-\mathbf{r}_{\text{c.m.}})\delta(\mathbf{r}_i-\mathbf{r}_{\text{c.m.}}-\mathbf{r})\delta(\mathbf{r}_j-\mathbf{r}_{\text{c.m.}}-\mathbf{r}')\right.\right. \\ &\quad \left.\left.-\sum_i\mathbf{r}\cdot(\mathbf{r}_i-\mathbf{r}_{\text{c.m.}})\delta(\mathbf{r}_i-\mathbf{r}_{\text{c.m.}}-\mathbf{r})\delta(\mathbf{r}_i-\mathbf{r}_{\text{c.m.}}-\mathbf{r}')\right|\Psi_0\right\rangle \\ &= -r^2\left\langle\Psi_0\left|\sum_i\delta(\mathbf{r}_i-\mathbf{r}_{\text{c.m.}}-\mathbf{r})\right|\Psi_0\right\rangle = -r^2\rho(\mathbf{r}) .\end{aligned} \tag{A5}$$

This result cancels the δ-function term in $S(\mathbf{r},\mathbf{r}')$ in Eq. (4.6), i.e., we have

$$\int d^3r'\mathbf{r}\cdot\mathbf{r}'S(\mathbf{r},\mathbf{r}')\sqrt{\rho_1(r)}\sqrt{\rho_1(r')}=0\ . \qquad \text{(A6)}$$

In our calculations we have found that both the sequential relation (4.14) and the relation (A6) are satisfied to an accuracy better than 1%.

[1] S. Gspann, in *Physics of Electronic and Atomic Collisions*, edited by S. Datz (North-Holland, Amsterdam, 1982), pp. 79 ff.

[2] E. Syskakis, F. Pobell, and H. Ullmaier, Phys. Rev. Lett. **55**, 2964 (1985).

[3] U. Helmbrecht and J. G. Zabolitzky, in *Monte Carlo Methods in Quantum Problems*, edited by M. Kalos (Reidel, Holland, 1984).

[4] V. R. Pandharipande, J. G. Zabolitzky, S. C. Pieper, R. B. Wiringa, and U. Helmbrecht, Phys. Rev. Lett. **50**, 1676 (1983).

[5] V. R. Pandharipande, S. C. Pieper, and R. B. Wiringa, Phys. Rev. B **34**, 4571 (1986).

[6] P. Sindzingre, M. J. Klein, and D. M. Ceperley, Phys. Rev. Lett. **63**, 1601 (1986).

[7] R. B. Wiringa, S. C. Pieper, and V. R. Pandharipande (unpublished).

[8] M. Casas and S. Stringari, J. Low. Temp. Phys. **79**, 135 (1990).

[9] M. V. Rama Krishna and K. B. Whaley, Phys. Rev. Lett. **64**, 1126 (1990); J. Chem. Phys. **93**, 746 (1990).

[10] M. V. Rama Krishna and K. B. Whaley, J. Chem. Phys. **93**, 6738 (1990).

[11] S. A. Chin and E. Krotscheck, Phys. Rev. Lett. **65**, 2658 (1990).

[12] A. Bohr and B. Mottelson, *Nuclear Structure* (Benjamin, New York, 1975), Vol. II.

[13] S. A. Chin and E. Krotscheck, Chem. Phys. Lett. **178**, 435 (1991).

[14] W. Kohn and P. Vashishta, in *Theory of the Inhomogeneous Electron Gas*, edited by S. Lundqvist and N. H. March (Plenum, New York, 1983), pp. 79 ff.

[15] E. Lieb, Phys. Rev. Lett. **46**, 457 (1990).

[16] H. J. Maris, in *Excitations in Two-Dimensional and Three-Dimensional Quantum Fluids*, Vol. 257 of *NATO Advanced Study Institute, Series B: Physics*, edited by A. F. G. Wyatt and M. J. Lauler (Plenum, New York, 1991).

[17] S. Stringari and J. Treiner, J. Chem. Phys. **87**, 5021 (1990).

[18] C. Ji and M. Wortis, Phys. Rev. B **34**, 7704 (1986).

[19] R. A. Aziz, V. P. S. Nain, J. C. Carley, W. L. Taylor, and G. T. McConville, J. Chem. Phys. **70**, 4330 (1990).

[20] C. Umrigar, K. Wilson, and J. Wilkins, Phys. Rev. Lett. **60**, 1719 (1990).

[21] D. Ceperly and M. Kalos, in *Monte Carlo Methods in Statistical Mechanics*, edited by K. Binder (Springer, New York, 1979).

[22] J. G. Zabolitzky, Prog. Part. Nucl. Phys. **16**, 103 (1986).

[23] P. J. Reynolds, D. M. Ceperley, B. J. Alder, and W. A. Lester, J. Chem. Phys. **77**, 5593 (1982).

[24] J. W. Moskowitz, K. E. Schmidt, M. E. Lee, and M. H. Kalos, J. Chem. Phys. **77**, 349 (1982).

[25] S. A. Chin, Phys. Rev. A **42**, 6991 (1990).

[26] M. Kalos, D. Levesque, and L. Verlet, Phys. Rev. A **9**, 2178 (1974).

[27] K. Schmidt, M. Kalos, M. Lee, and G. Chester, Phys. Rev. Lett. **45**, 573 (1990).

[28] C. E. Campbell, Phys. Lett. **44A**, 471 (1973); C. C. Chang and C. E. Campbell, Phys. Rev. B **15**, 4238 (1977); E. Krotscheck, *ibid.* **33**, 3158 (1986).

[29] E. Krotscheck, Q.-X. Qian, and W. Kohn, Phys. Rev. B **31**, 4245 (1985).

[30] R. P. Feynman, Phys. Rev. **94**, 262 (1990).

[31] E. Krotscheck, Phys. Rev. B **31**, 4258 (1985).

[32] L. Van Hove, Phys. Rev. **95**, 249 (1990).

[33] R. Schiavilla, D. Lewart, V. Pandharipande, S. Pieper, R. Wiringa, and S. Fantoni, Nucl. Phys. **A473**, 267 (1987).

[34] R. Barnett, P. Reynolds, and W. Lester, Jr., J. Comput. Phys. **96**, 258 (1991).

[35] C. C. Chang and C. E. Campbell, Phys. Rev. B **13**, 3779 (1976).